Mechanogeometry of nanowrinkling in cholesteric liquid crystal surfaces

Ziheng Wang,[*] Phillip Servio,[†] and Alejandro D. Rey[‡]
Department of Chemical Engineering, McGill University, 3610 University Street, Montréal, Québec H3A 0C5, Canada

(Received 19 September 2019; accepted 3 April 2020; published 19 June 2020)

Biological plywoods are multifunctional fibrous composites materials, ubiquitous in nature. The chiral fibrous organization is found in chitin (insects), cellulosics (plants), and collagen I (cornea and bone of mammals) and is a solid analog of that of cholesteric liquid crystals. The surface and interfaces of plywoods are distinguished by hierarchical topographies and nanowrinkling. In this paper, we present a theory to model the emergence of these surfaces and interfaces using liquid crystal-based shape equations that directly connect material properties with geometric wrinkling. The model applies to liquid crystal precursors of the plywood solid analoges. We focus on wrinkling geometry, wrinkling mechanics, and the mechanogeometry relationships that underlie multifunctionality ubiquitous in biological surfaces. Scaling wrinkling laws that connect mechanical pressures and stresses to folding and bending are formulated and quantified. A synthesis of the connections between mechanics and geometry is achieved using the topology of stress curves and curvature of the wrinkles. Taken together the results show that anchoring is a versatile surface morphing mechanism with a rich surface bending stress field, two ingredients behind many potential multifunctionalities.

DOI: 10.1103/PhysRevE.101.062705

I. INTRODUCTION

Cholesteric liquid crystalline phase can be widely found throughout nature [1–4]. A distinguishing difference between cholesteric liquid crystals (CLCs) and other liquid crystal [5] is that CLCs are macroscopically (μm-range) chiral with a spatially periodic structure, which ensures the existence of some unique properties such as optical [6] and tribological [7] response. The cholesteric material is characterized by the orientation of the helix vector, the handedness $(+/-)$, and the pitch (periodicity) length P_0 [3]. The pitch P_0 dependence on chemical and electromagnetic fields is the source of rich sensor and actuator capabilities. In this work we focus on the interaction of the orientation structure of cholesteric helix with the geometry of a free surface and seek to elucidate the coupling mechanisms between elastic pressures generated from surface orientation gradients and surface wrinkling geometry. Since cholesterics have periodic structures one finds periodic wrinkling, but as we show in this work the observed geometric periodicity depends on the anisotropy of the surface tension, generally known as anchoring [8–10]. In particular in this paper we explore how symmetry breaking from higher-order harmonics in the anisotropic surface tension creates more complex wrinkling than a single sinusoidal profile.

To describe wrinkling in anisotropic soft matter surfaces we use the capillary vector methodology. The capillary vector method is widely used in crystalline and hard matter, which, after modification, can also be applied to soft matter materials and processes such as the analysis of Rayleigh fiber instabilities in liquid crystals [13], triple lines [14], wetting, and more [10]. In this paper, we extend this method to predict wrinkling patterns found in CLC-free surfaces, given a certain unit vector director field $\mathbf{n}$, which characterizes the main average molecular orientation. The Cahn-Hoffman capillary vector [15,16] $\boldsymbol{\Xi} := \nabla(r\gamma)$ is defined by the gradient of the product between the magnitude of position vector $\mathbf{r}$ and surface energy γ, and is the core element of this paper. The Cahn-Hoffman capillary vector method yields analogies and direct correspondences in many fields and processes. For example, the Maxwell-Lamé equation [17] in optical-elasticity research has the same form as Eq. (28) in this paper, which is related to the principal surface stresses. On large spatial scales, we find that geological pattern formation is described by ad hoc geometric relations [18], that emerge naturally in the Cahn-Hoffman capillary vector method formulated here.

Figure 1 is a schematic explaining the wrinkling geometry and mechanical quantities associated with folding. Given a periodic director field $\mathbf{n}(x)$, we can observe an undulating surface profile $h(x)$, whose intrinsic geometry can be described by its curvature κ. The disclination defects [19] (red λ^+ points) separate the CLC into two regions: distorted surface region above which surface wrinkling occurs, and bulk region where $\mathbf{n}(x)$ is the director field corresponding to a cholesteric liquid crystal with pitch P_0. Since the surface tension is anisotropic, the Cahn-Hoffman capillary vector $\boldsymbol{\Xi}$ describing the capillarity and surface is a 2D planar (no torsion is considered) surface vector acting on a surface with outward unit normal $\mathbf{k}$ and unit tangent vector $\mathbf{t}$. The surface stress vector normal to $\boldsymbol{\Xi}$ is $\mathbf{T}_v$. The surface is flat along direction $\mathbf{k} \times \mathbf{t}$ with vanishing Gaussian curvature. The geometric frame $(\mathbf{t}, \mathbf{k})$ defines a unit square area (gray) and the mechanical frame $(\boldsymbol{\Xi}, \mathbf{T}_v)$ defines another square area (blue) and the connection between geometry and mechanics, which is a central topic in this paper, is the rotation-dilation Jacobian matrix that transforms $(\mathbf{t}, \mathbf{k})$ into $(\boldsymbol{\Xi}, \mathbf{T}_v)$.

[*]ziheng.wang@mail.mcgill.ca
[†]phillip.servio@mcgill.ca; http://hydratetech.com/
[‡]alejandro.rey@mcgill.ca; http://mmrg.chemeng.mcgill.ca/

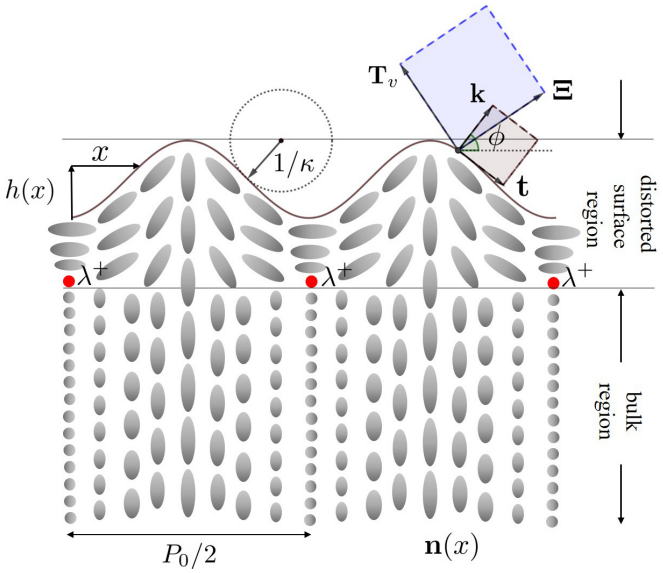

FIG. 1. Schematic of surface wrinkling of a cholesteric liquid crystal; surface relief $[h(x)]$, geometric frame $(\mathbf{t}, \mathbf{k})$, surface curvature (κ), surface mechanical fields $(\Xi, \mathbf{T}_v)$; $\mathbf{t}$ is the unit surface tangent vector, $\mathbf{k}$ is the outward unit normal, Ξ is the capillary vector, and $\mathbf{T}_v$ is the surface stress vector. Far from the interface, the cholesteric helix unit vector $\mathbf{H} = \hat{\boldsymbol{\delta}}_x$ is horizontal and the director field is a pure twist: $\mathbf{n}(x) = (0, n_y, n_z)$; $\mathbf{n} \cdot \mathbf{H} = 0$. In the interfacial region the helical director field uncoils $\mathbf{n}(x) = (n_x, n_y, 0)$ into a planar splay-bend director field and $\mathbf{n} \cdot \hat{\boldsymbol{\delta}}_z = 0$. The surface and bulk region are separated by an array of low-energy nonsingular λ^+ disclination lines [11,12]. The chirality of the bulk director is transferred to the surface director in terms of spatial gradient information. The surface curvature is periodic and the period is equal to half the cholesteric pitch $P_0/2$. Capillary vector Ξ generalizes the surface tension under anisotropy. A counterclockwise rotation of Ξ gives the stress vector $\mathbf{T}_v$. The orthonormal geometrical frame $(\mathbf{t}, \mathbf{k})$ is related to the orthogonal mechanical frame $(\Xi, \mathbf{T}_v)$ by a dilation-rotation transformation, as shown in this paper.

In our previous work [11,12] we first explored wrinkling in CLC surfaces with a simple quadratic anisotropic surface tension known as the Rapini-Papoular model [20]. The key mechanism for wrinkling is based on the fact that energy is minimized with a specific relative angle between the director field $\mathbf{n}$ and the unit surface normal $\mathbf{k}$, or equivalently $(\mathbf{n} \cdot \mathbf{k})$. If the surface director orientation changes $\mathbf{n}(x)$ since CLC are spatially periodic, then the surface energy is then minimized by geometric distortions $\mathbf{k}(x)$, that seek to keep the optimal (lowest energy) relative angle between $\mathbf{t}$ and $\mathbf{n}$. Subsequently, inspired by actual surface material properties of liquid crystals, we found that a more complex surface pattern can be described including a higher-order quartic term $(\mathbf{n} \cdot \mathbf{k})^4$ in the Rapini-Papoular equation [11,12]. This previous work [11,12] showed that to describe experimentally observed two-scale wrinkling, anchoring mechanisms are sufficient and that membrane-anchoring models [21] that also predict two-scale wrinkling are not always necessary. The latter class of membrane-LC models have two intrinsic length scales (membrane scale and helix pitch) whose ratio defines a folding number; increasing the folding number increases the number of wrinkling length scales, leading to predictions in agreement with the structure of the queen of the night tulip. These membrane-liquid crystal models rely on compressive stress loading to create wrinkling, while the purely anchoring models considered in this paper fold the surface to reduce surface tension.

The formal calculation of wrinkling geometry is based on the solution of the shape equation that essentially balances the capillary pressures with the bulk stress jump [10]. When the latter is zero, the curvature is the ratio of the driving capillary pressure divided by a resistance coefficient. The driving pressure for wrinkling is the director pressure which is unique to liquid crystal surfaces since it originates in surface director gradients $\nabla_s \mathbf{n}$. The origin and underlying nature of this unique but less recognized pressure can be elucidated by using mechanical conservation principles such as least action methods, as done in this paper. The wrinkling formation process is characterized by the surface geometry and the surface stress field. The surface geometry includes the surface relief $h(x)$ and more importantly its first four moments, including skewness and kurtosis [22]. Of special interest to this present paper is predict and compare higher-order surface relief moments generated from soft matter elastic instabilities with those of hard materials obtained from abrasion, laser treatments and more [23–25]. Geometric analysis on its own does not shed light on mechanical driving forces and interfacial stresses. Of particular importance to this present paper is to know and assess the principal stresses that drive wrinkling and construct an atlas of complex Lamé curves [26] that synthesize the action of the stresses involved. For isotropic surfaces one expects a stress circle, for low order anisotropic surfaces one would expect elliptical Lamé stress curves, but for higher-order anisotropy, stress curve intersections are inevitable and reveal the nature of the underlying forces. Last, integrating geometry and mechanics, as done in other systems under the name of geometromechanics, provides the direct link between surface curvature and principal stresses and encapsulates in one diagram why and how wrinkling emerges.

Based on the above observations and facts, the main objectives of this paper are: (1) Derive complementary Maxwell-Lamé and least action method that lead to the shape equation, highlighting the essential nature of the driving director capillary pressure and its dependence on quadratic and quartic anchoring energies. (2) Characterize the full statistical geometry of wrinkling, including skewness and kurtosis as a function of anchoring, emphasizing connections with hard material surfaces. (3) Present an atlas of Lamé principal stress curves as a function of anchoring, to highlight the mechanical forces behind wrinkling. (4) Present an integrated mechanogeometry characterization in terms of curvature and surface stress ratio, that augments the understanding obtained from just solving the shape equation.

In this paper, we use the following assumptions: (1) The CLC surface is an infinite 1D manifold where the Gaussian curvature vanishes (parabolic surfaces). This means we study a periodic planar 2D space curve instead of a 2D surface. The invariance in third dimension is commonly found in nature [27,28]. (2) The model is time-independent and focuses on equilibrium patterns and not on transients that may include convective, Marangoni [29,30] or back flows (energy

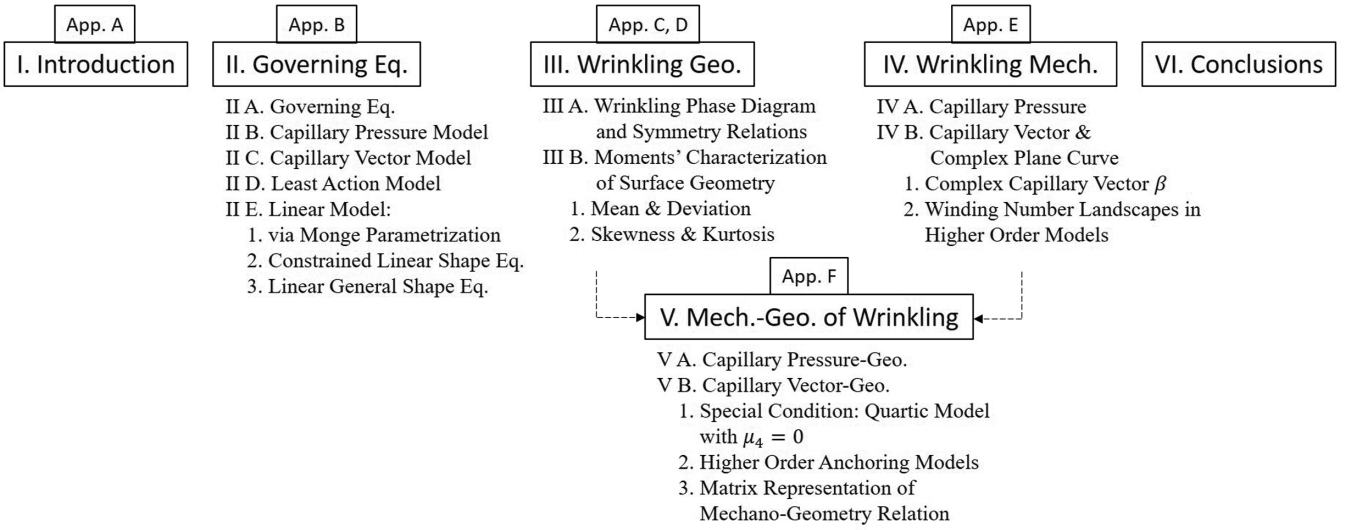

FIG. 2. Organization and flow of information in this paper. App. denotes Appendix. Geo. denotes geometry, and Mech. denotes mechanics.

minimization analysis is included); an energy minimization is included. (3) The surface director field $\mathbf{n}(x)$ is known a priory and based on our previous work and experimental data [31]. (4) Bulk elasticity, known as the elastic correction is negligible as shown previously and corresponds to the "easy shape" condition that emerges under zero net capillary pressures. Phenomena and materials inconsistent with these assumptions are not described in this work and are beyond the scope of this paper. The main focus of this paper is on anchoring energies up to quartic order, but few generalizations to six order anchoring are presented when they shed important insights.

This paper is organized as follow (see Fig. 2 for specific details). In Sec. II, we derive the governing equation that controls the shape of the surface. Then the shape equation will be discussed in terms of three different but complementary models: (1) the capillary pressure model, (2) the Maxwell-Lamé capillary vector model, and (3) the least action model. Each of them provides complementary insights, specially on the driving force (director pressure) and principal stresses; we note that these three models are consistent and equivalent and their solutions predict the same wrinkling. At the end of Sec. II, a linear model is formulated and solved to approximate wrinkling patterns with less numerical computation but with high accuracy, revealing parametric dependence and scaling laws. In Sec. III, we evaluate the statistical geometry of the patterns, including skewness and kurtosis as a function of anchoring [12]. Section IV presents a mechanical characterization in terms of principal stress components and Lamé curves. Section V presents the mechanogeometry in terms of curvature and principal stress ratio which is an efficient method to explain and quantify wrinkling geometry. A mechanogeometry transformation matrix containing the information of both geometry and mechanics is also analyzed in the end of this section. Section V also serves as a bridge between Secs. III and IV. Section VI presents the conclusions. Complete mathematical derivations and proofs and supporting information are included in the Appendices (App. in Fig. 2). We emphasize that under the conditions of this study, wrinkling emerges if and only if the geometric distortions reduce energy as compared with a pure flat geometry with the same director field. In Appendix A, we prove that the total surface energy density does decrease by forming wrinkling patterns.

The main contribution of this paper is that it explains and characterizes nanowrinkling using geometry, mechanics, and the intrinsic connection between these two descriptions. It also encourages potential applications. For example, one of the key points in tissue engineering is to control the growth of cells on a biocompatible scaffold. The growth of cells is shown to be dependent on the geometry of the scaffolds [32]. If we want to control tissue growth, then we need to characterize the stress field along the scaffold surface, which is difficult to measure. However, various techniques such as electron microscopy can be used to measure the surface profile, which, in this paper, is shown to be related to the stress field, through the mechanogeometry couplings. The natural biocompatibility of biological plywood allows it to be applied in tissue engineering in the future and is also a main contribution of this paper.

II. GOVERNING EQUATIONS

A. Governing equation

The generalized Rapini-Papoular equation [33,34] describes the interfacial energy γ by either Legendre polynomials $\gamma = \sum_j \mu_{2j} \cos^{2j}\theta$, Fourier series $\gamma = \sum_j \mu_{2j} \cos 2j\theta$, or Jacobi elliptic function $\gamma = \frac{W}{2}\,\mathrm{sn}^2(\theta, c)$, where $0 \leqslant c \leqslant 1$ is the modulus of the elliptic function. We will show later that higher-order harmonics will introduce new wavelengths rather than creating new wrinkling phenomena. Hence, we will use the following Legendre polynomial form, which is consistent with the original paper [33]:

$$\gamma = \gamma_0 + \sum_{j=1}^{\infty} \mu_{2j} (\mathbf{n} \cdot \mathbf{k})^{2j}, \tag{1}$$

where γ_0 is the isotropic surface energy and μ_{2i} $(i = 1, 2, \ldots, j)$ are the anchoring coefficients influenced by factors such as temperature, surfactants, and more. As mentioned above, $\mathbf{n}$ is the director vector, $\mathbf{k}$ is the surface outward unit

normal, and P_0 is the helix pitch. The parameters of the model are integrated into a vector $\mathbf{V} = [\boldsymbol{\mu}\ P_0]$ such that $\boldsymbol{\mu} = [\mu_2\ \mu_4\ \ldots\ \mu_{2n}] \in \Lambda_{2n}$ and $P_0 \in \mathcal{P}$, where Λ is the space spanned by independent variables μ_2, $\mu_4 \ldots\ \mu_{2n}$ with dimension n used for convenience, and $\mathcal{P}$ is also introduced for convenience. Hence, the parametric space is $\Lambda_{2n} \oplus \mathcal{P} \cong \mathbb{R}^{n+1}$. The order of the wrinkling model is defined by the maximum $2n$, with $n = 1$ denoted quadratic and $n = 2$ the quartic model. As mentioned above, higher-order models with lower symmetry have the potential to create more complex wrinkling, but no extensive data appears to be available for higher-order coefficients. In this paper we mainly focus on the quartic ($n = 2$) model where the anchoring coefficient vector is $\boldsymbol{\mu} = [\mu_2\ \mu_4]$, but generalized results are provided when available or when revealing novel results. The symmetry properties of surface wrinkles in terms of the signs of P_0 and $\boldsymbol{\mu} = [\mu_2\ \mu_4]$ was discussed previously [11,12].

For completeness we first very briefly presents the bulk elasticity, which becomes nonnegligible in surface wrinkling under very short pitches, as in blue phases not considered here. The Oseen-Frank bulk elastic energy density $f_g(\mathbf{n}, \nabla\mathbf{n})$ for a CLC surface reads [35]

$$2f_g = K_1(\nabla\cdot\mathbf{n})^2 + K_2(\mathbf{n}\cdot\nabla\times\mathbf{n} - q)^2 + K_3(\mathbf{n}\times\nabla\times\mathbf{n})^2 + (K_2 + K_4)[\mathrm{tr}(\nabla\mathbf{n})^2 - (\nabla\cdot\mathbf{n})^2], \tag{2}$$

where $K_i (i = 1, 2, 3)$ are the splay, twist, and bend elastic constants, while K_4 is the saddle-splay elastic constant. The one-constant approximation is commonly used in the literature for low molar mass liquid crystals [35], which allows to set $K_1 = K_2 = K_3 = K$ while $K_4 = 0$, and in this paper allows us to obtain analytical solutions that capture the origin of nanowrinkling in cholesteric surfaces with an uncoiled director field. If $q = 0$, then f_g can be written simply by

$$\begin{aligned} 2f_g &= K[(\nabla\cdot\mathbf{n})^2 + \underbrace{(\mathbf{n}\cdot\nabla\times\mathbf{n})^2 + (\mathbf{n}\times\nabla\times\mathbf{n})^2}_{(\nabla\times\mathbf{n})^2} \\ &\quad + \underbrace{\mathrm{tr}(\nabla\mathbf{n})^2 - (\nabla\cdot\mathbf{n})^2}_{\nabla\cdot[(\mathbf{n}\cdot\nabla)\mathbf{n} - \mathbf{n}(\nabla\cdot\mathbf{n})]}] \\ &= K\|\nabla\mathbf{n}\|^2. \end{aligned} \tag{3}$$

The gradient interfacial free-energy density γ_g is computed by using geometric tensor $\mathbf{g} := (\mathbf{n}\cdot\nabla)\mathbf{n} - \mathbf{n}(\nabla\cdot\mathbf{n})$ as [36]

$$\gamma_g = \tfrac{1}{2}(K_2 + K_4)\mathbf{k}\cdot\mathbf{g}. \tag{4}$$

As mentioned above, the Cahn-Hoffman capillary vector [15,16] is defined by $\boldsymbol{\Xi} := \nabla(r\gamma)$, where r is the magnitude of position vector $\mathbf{r}$. $\boldsymbol{\Xi}$ describes the thermodynamics of an interface, which can be decomposed along vector $\mathbf{k}$ and $\mathbf{t}$ such that normal capillary vector $\boldsymbol{\Xi}_\perp = \Xi_\perp\mathbf{k}$ and tangent capillary vector $\boldsymbol{\Xi}_\parallel = \Xi_\parallel\mathbf{t}$. Notice that $d(r\gamma) = \nabla(\mathbf{r}\gamma)\cdot d\mathbf{r}$ so we have

$$rd\gamma + \gamma dr = \boldsymbol{\Xi}\cdot d(r\mathbf{k}) = r\boldsymbol{\Xi}\cdot d\mathbf{k} + \boldsymbol{\Xi}\cdot\mathbf{k}dr. \tag{5}$$

Equation (5) yields, for the quartic model, two components,

$$\boldsymbol{\Xi}_\perp = \gamma\mathbf{k} = \gamma_0\mathbf{k} + [\mu_2 + \mu_4(\mathbf{nn}:\mathbf{kk})](\mathbf{nn}:\mathbf{kk})\mathbf{k}, \tag{6}$$

$$\boldsymbol{\Xi}_\parallel = \mathbf{I}_s\cdot\frac{\partial\gamma}{\partial\mathbf{k}} = [2\mu_2 + 4\mu_4(\mathbf{nn}:\mathbf{kk})](\mathbf{nn}:\mathbf{kt})\mathbf{t}, \tag{7}$$

where $\mathbf{I}_s = \mathbf{I} - \mathbf{kk}$ is the surface dyadic and $\mathbf{I}$ the unit dyadic. We note that if μ_2 appears in the normal vector in Eq. (6) then $2\mu_2$ appears in the tangential vector in Eq. (7) and the same for μ_4. This multiplicative effect affects wrinkling. Also the quartic anchoring in Eqs. (6) and (7) is modulated by ($\mathbf{nn}$: $\mathbf{kk}$), introducing nonlinearity into the quartic coefficient.

The interfacial static force balance requires that the following equation holds on CLC/air interface [29,37,38]:

$$-\mathbf{k}\cdot(\mathbf{T}^a - \mathbf{T}^b) = \nabla_s\cdot\mathbf{T}_s, \tag{8}$$

where $\mathbf{T}^{a/b}$ represent the total stress tensor in the air (a) and in the bulk (b) of CLC phase. $\nabla_s = \mathbf{I}_s\cdot\nabla$ is the surface gradient operator and $\mathbf{T}_s$ is the interface stress tensor. $\mathbf{T}^{a/b}$ are given by

$$\mathbf{T}^a = -p^a\mathbf{I}, \tag{9}$$

$$\mathbf{T}^b = -(p^b - f_g)\mathbf{I} + \mathbf{T}^E, \tag{10}$$

where $p^{a/b}$ are the hydrostatic pressures. The Ericksen stress tensor $\mathbf{T}^E$ is given by

$$\mathbf{T}^E = -\frac{\partial f_g}{\partial\nabla\mathbf{n}}\cdot(\nabla\mathbf{n})^\intercal. \tag{11}$$

The projection of Eq. (8) along $\mathbf{k}$ yields the well-known shape equation

$$\underbrace{(p^a - p^b) + f_g + \mathbf{kk}:\left[-\frac{\partial f_g}{\partial\nabla\mathbf{n}}\cdot(\nabla\mathbf{n})^\intercal\right]}_{\text{Stress Jump, SJ}} = \underbrace{\nabla_s\cdot\mathbf{T}_s\cdot\mathbf{k}}_{-p_c}, \tag{12}$$

where stress jump (SJ) is the total normal stress jump, and p_c is the capillary pressure. Assume $p^a - p^b = 0$ and denote the rest of the term on the left-hand side as the elastic correction. We next show that for the case at hand we can safely neglect SJ. Recall the interfacial torque balance equation [36,39]

$$-\mathbf{h} + \mathbf{k}\cdot\frac{\partial f_g}{\partial\nabla\mathbf{n}} = \lambda^s\mathbf{n}, \tag{13}$$

where λ^s is the Lagrangian multiplier and $\mathbf{h}$ is the surface molecular field composed by two parts,

$$\mathbf{h} = \underbrace{-\frac{\partial\gamma_{\mathrm{an}}}{\partial\mathbf{n}}}_{\mathbf{h}_{\mathrm{an}}}\underbrace{-\frac{\partial\gamma_g}{\partial\mathbf{n}} + \nabla_s\cdot\left(\frac{\partial\gamma_g}{\partial\nabla_s\mathbf{n}}\right)}_{\mathbf{h}_g}, \tag{14}$$

where $\mathbf{h}_{\mathrm{an}}$ is the anisotropic component and $\mathbf{h}_g$ is related to the gradient. Multiply by $(\nabla\mathbf{n})^\intercal$ on both sides of Eq. (13). The torque balance equation can be rewritten as

$$-\mathbf{h}\cdot(\nabla\mathbf{n})^\intercal + \mathbf{k}\cdot\mathbf{T}^E = \mathbf{0}, \tag{15}$$

which implies that surface director torque is balanced by the bulk stress force. Thus, we can compute $\mathbf{kk}:\mathbf{T}^E$ by $\mathbf{hk}:(\nabla\mathbf{n})^\intercal$,

$$\mathbf{hk}:(\nabla\mathbf{n})^\intercal = \left[-\frac{\partial\gamma_{\mathrm{an}}}{\partial\mathbf{n}} - \frac{\partial\gamma_g}{\partial\mathbf{n}} + \nabla_s\cdot\left(\frac{\partial\gamma_g}{\partial\nabla_s\mathbf{n}}\right)\right]\cdot(\nabla\mathbf{n})^\intercal\cdot\mathbf{k}, \tag{16}$$

which in our case vanishes (see Appendix A). The remaining contribution to SJ contributes less than 2% to the shape equation and is not significant if P_0 is greater than 1 μm [20]. Thus the shape Eq. (12) reduces to a vanishing total capillary pressure $p_c = 0$.

We parametrize the relevant vector fields as follows: $\mathbf{n} = [\cos qx \ \sin qx]$, $\mathbf{t} = [\sin\phi \ -\cos\phi]$ and $\mathbf{k} = [\cos\phi \ \sin\phi]$, where the rectangular coordinate frame (x, y) is fixed. The adopted planar surface director field $\mathbf{n}(x)$ is discussed in our previous work and suggested by actual experiments. Here $q = 2\pi/P_0$ is the wave vector and the actual director angle qx is linear in x. Nonlinear director fields lead to tangentially graded wrinkling, explored previously for the quadratic model [40].

B. Capillary pressure model

Here we briefly present the standard shape Eq. (12) in terms of the capillary pressures using the capillary vector Eqs. (6) and (7) and its special relation with the surface stress tensor $\mathbf{T}_s$ (see Appendix B) [41]. For our cylindrical surface ($\mathbf{I}_s = \mathbf{tt}$) the relation between stress tensor $\mathbf{T}_s$ and Cahn-Hoffman capillary vector $\boldsymbol{\Xi}$ is

$$\mathbf{T}_s = \boldsymbol{\Xi}\cdot(\mathbf{ktt} - \mathbf{ttk}) = \underbrace{\Xi_\perp \mathbf{tt}}_{\mathbf{T}_N} \underbrace{-\Xi_\parallel \mathbf{tk}}_{\mathbf{T}_B}, \tag{17}$$

where $\mathbf{T}_N$ is the normal stress component and $\mathbf{T}_B$ is the bending stress component. Bending stresses are characteristic of LC surfaces and interfaces due to anchoring and reflect the fact that the surface energy can be changed through area rotations [10]. The sign of $\mathbf{T}_B$ is opposite to that of $\boldsymbol{\Xi}_\perp$ because bending stress is positive when creating negative curvature while $\boldsymbol{\Xi}_\perp$ is along the outward unit normal $\mathbf{k}$. The stress vector $\mathbf{T}_v$ acting on the surface edge is

$$\mathbf{T}_v = \mathbf{t}\cdot\mathbf{T}_s = \Xi_\perp \mathbf{t} - \Xi_\parallel \mathbf{k} = \boldsymbol{\Xi}\cdot\mathbf{R}, \tag{18}$$

where $\mathbf{R}$ is the rotation matrix corresponding to an counterclockwise $\pi/2$ rotation along the $\mathbf{b} = \mathbf{t}\times\mathbf{k}$ direction such that $\mathbf{R} = \mathbf{tk} - \mathbf{kt}$. If we replace Eq. (12) with Eq. (17), then shape equation in the language of capillary pressures reads [36]

$$p_c = \nabla_s\cdot\boldsymbol{\Xi} = \underbrace{\frac{\partial\boldsymbol{\Xi}_\perp}{\partial\mathbf{k}} : \nabla_s\mathbf{k}}_{\text{dilation}} + \underbrace{\frac{\partial\boldsymbol{\Xi}_\parallel}{\partial\mathbf{k}} : \nabla_s\mathbf{k}}_{\text{rotation}} + \underbrace{\frac{\partial\boldsymbol{\Xi}_\parallel}{\partial\mathbf{n}} : \nabla_s\mathbf{n}}_{\text{director}}, \tag{19}$$

where $(\partial_{\mathbf{n}}\boldsymbol{\Xi}_\perp : \nabla_s\mathbf{n})$ vanishes since γ is a function of $(\mathbf{n}\cdot\mathbf{k})$. Equation (19) shows that there are three distinct capillary pressures. The first term on the right-hand side characterizes the capillary pressure due to area change denoted by dilation pressure P_{dil}, which is the standard Laplace pressure. The second term is the rotation pressure P_{rot} due to area rotation relative to a given director field. In crystal surfaces this pressure is denoted by Herring's pressure. The last term is the director capillary pressure P_{dir}, which is the driving force that causes wrinkling patterns and is generated by surface director gradients and is unique to liquid crystals [10].

Expanding Eq. (19) we obtain a nonlinear first-order ODE for the surface normal angle ϕ,

$$\frac{\kappa}{\sin\phi} = \frac{d\phi}{dx} = \frac{1}{\sin\phi}\frac{F_{\text{Dr}}}{F_{\text{Rs}}}, \tag{20}$$

where κ is the surface curvature defined by $d\phi/ds$ and s is the arc-length. In Eq. (20) the driving force F_{Dr} and resistance F_{Rs} are expressed in the quartic model by

$$F_{\text{Dr}} = 2[\mu_2 + 2\mu_4(\mathbf{nn}:\mathbf{kk})]\left(\mathbf{n}\otimes\frac{\partial\mathbf{n}}{\partial s} : \mathbf{tk}\right) + 2[\mu_2 + 6\mu_4(\mathbf{nn}:\mathbf{kk})]\left(\mathbf{n}\otimes\frac{\partial\mathbf{n}}{\partial s} : \mathbf{kt}\right), \tag{21}$$

$$F_{\text{Rs}} = \gamma_0 + \mu_2[2(\mathbf{nn}:\mathbf{tt}) - (\mathbf{nn}:\mathbf{kk})] + 3\mu_4(\mathbf{nn}:\mathbf{kk})[4(\mathbf{nn}:\mathbf{tt}) - (\mathbf{nn}:\mathbf{kk})]. \tag{22}$$

The boundary condition for the first-order ODE Eq. (20) is $\phi|_{x=0} = \pi/2$. Also notice that $\mathbf{nn}:\mathbf{tt} + \mathbf{nn}:\mathbf{kk} = 1$ so $\mathbf{n}\cdot\mathbf{t}$ and $\mathbf{n}\cdot\mathbf{k}$ are not independent in the case of the planar splay-bend surface director field studied here. Equation (20) implies that surface curvature κ is measured by the quotient between F_{Dr} and F_{Rs}. It can be verified that

$$\int_0^{P_0}\frac{F_{\text{Dr}}}{F_{\text{Rs}}}\,ds = 0, \tag{23}$$

guaranteed by Gauss-Bonnet theorem. Finally, surface relief h can be computed by

$$h(s) = -\int_0^s \cot\phi(x)\,dx. \tag{24}$$

We note that to convert $h(s)$ to $h(x)$ or any other function $x(s)$ we just use $dx = ds\sin\phi$.

C. Capillary vector model

Defining $\mathbf{b} = \mathbf{t}\times\mathbf{k}$, a Frenet-Serret frame can be constructed,

$$\frac{d}{ds}\begin{bmatrix}\mathbf{t}\\ \mathbf{k}\\ \mathbf{b}\end{bmatrix} = \begin{bmatrix}0 & \kappa & 0\\ -\kappa & 0 & \tau\\ 0 & -\tau & 0\end{bmatrix}\begin{bmatrix}\mathbf{t}\\ \mathbf{k}\\ \mathbf{b}\end{bmatrix}, \tag{25}$$

where τ represents torsion which is 0 in this paper as we only consider planar curves. Next we apply Frenet-Serret frame and rewrite Eq. (19) as follows:

$$\nabla_s\cdot\boldsymbol{\Xi} = \left[\left(\frac{\partial\Xi_\parallel}{\partial s} - \kappa\Xi_\perp\right)\mathbf{t} + \left(\frac{\partial\Xi_\perp}{\partial s} + \kappa\Xi_\parallel\right)\mathbf{k}\right]\cdot\mathbf{t}. \tag{26}$$

Using the relative angle $\theta = \phi - qx$, there is an alternating structure,

$$\frac{\partial\Xi_\perp}{\partial\theta} + \Xi_\parallel = 0, \tag{27}$$

which relates the principal stress components $(\Xi_\parallel, \Xi_\perp)$. Since the magnitude of $\Xi_\perp$ is γ, we are able to link surface energy with surface curvature by a single expression,

$$\Upsilon(\gamma) = \kappa, \quad \text{where } \Upsilon(\gamma) = -\frac{1}{\gamma}\frac{\partial}{\partial s}\left(\frac{\partial\gamma}{\partial\theta}\right). \tag{28}$$

Equation (28) is the general shape equation. It is a general form not only because γ is not explicitly expressed but also shares common structure with Maxwell-Lamé equation in the study of optical-elasticity [17]. If we denote $\Sigma = ds/d\theta$, then Σ is just a coordinate transformation and Eq. (28) is a second-order ordinary differential equation. In Sturm-Liouville form

it reads

$$\frac{d}{ds}\left(\frac{d\gamma}{ds}\right)+\kappa\Sigma^{-1}\gamma=0. \tag{29}$$

Comparing the two versions of the shape Eqs. (19) and (28) we can see that the capillary pressure model highlights the role of director pressure $P_{\rm dir}$ [Eq. (19)] and the Maxwell-Lamé model [Eqs. (26) and (27)] highlights the principal stresses. Finally, Eq. (29) shows the Laplacian ∇^2 in arc-length space of the surface energy γ is proportional to the capillary dilation pressure $\kappa\gamma$ and hence periodicity in γ is connected to periodicity in κ.

D. Least action model

Last, we recast the shape equation into a least action model by identifying the wrinkling Hamiltonian. Consider the following functional S_L reaching extremum:

$$S_L=\int\mathcal{L}\,ds=\int\left[\frac{1}{2}\left(\frac{d\gamma}{ds}\right)^2-\frac{1}{2}\kappa\Sigma^{-1}\gamma^2+\pounds(s)\right]ds. \tag{30}$$

The Legendre transformation of $\mathcal{L}$ is

$$\begin{aligned}\mathcal{H}&=\frac{d\gamma}{ds}\frac{\partial\mathcal{L}}{\partial\left(\frac{d\gamma}{ds}\right)}-\mathcal{L}\left(\gamma,\frac{d\gamma}{ds},s\right)\\&=\frac{1}{2}\left(\frac{d\gamma}{ds}\right)^2+\frac{1}{2}\kappa\Sigma^{-1}\gamma^2-\pounds(s).\end{aligned} \tag{31}$$

Equation (31) can be considered as the energy of this system. Comparing Eq. (31) with the standard equation of a driven pendulum, we found that $d\gamma/ds$ is the wrinkling velocity of the surface, and $\kappa\Sigma^{-1}$ represents its modulus. We then consider $\mathcal{H}$ as the wrinkling Hamiltonian of a CLC surface. It can be verified that its corresponding wrinkling Lagrangian $\mathcal{L}$ satisfies the Euler-Lagrange equation. Then shape Eq. (29) is simply generated by a variation $\delta S_L=0$. Each component of $\mathcal{H}$ represents important aspects of wrinkling. The velocity $d\gamma/ds$ tells us how fast the energy changes along s, and κ reflects how curved the surface is, while Σ is just a coordinate transformation so that the first two terms of $\mathcal{H}$ have the same dimension. $\kappa\Sigma^{-1}\gamma^2$ corresponds to a potential energy stored by the surface. In addition, $\pounds(s)$ corresponds to the driving force. It can be verified numerically that $\pounds(s)$ is just the scaled director pressure $P_{\rm dir}$ [see Eq. (19)]. The least action model of cholesteric wrinkling shows that anisotropic capillary phenomena can be projected into a pendulum-like equation, as done in isotropic systems.

E. Linear model

Linearization leads to solvable shape equations that yield explicit formulas for geometry, mechanics, and mechano-geometry relationships. It turns out that the capillary vector [Eqs. (6) and (7)], the capillary pressure model (Sec. II B), and the capillary vector model (Sec. II C) can be independently linearized giving complementary computational tools and insights. We use an upper tilde to denote linearized quantity and a star subscript for a quantity which is scaled by γ_0. Here we focus on the quartic model $\gamma=\gamma_0+\mu_2(\mathbf{n}\cdot\mathbf{k})^2+\mu_4(\mathbf{n}\cdot\mathbf{k})^4$ for concreteness.

1. Linear model via Monge parametrization

Consider an almost-flat surface, naturally there is a trivial solution where $\boldsymbol{\Xi}$ is a constant solution to equation $\nabla_s\cdot\boldsymbol{\Xi}=0$. Without loss of generality we can choose $\boldsymbol{\Xi}=\gamma_0\hat{\boldsymbol{\delta}}_y$ which indicates that at $x=s=0$ the capillary vector [Eqs. (6) and (7)] is along the y axis. Using a Monge parametrization of the surface $\mathbf{r}=[x,h(x)]$, the tangent unit vector $\mathbf{t}$ in the linear regime is

$$\mathbf{t}\approx[1\quad\nabla_\parallel h]. \tag{32}$$

Multiply $\mathbf{t}$ on both sides of $\boldsymbol{\Xi}=\gamma_0\hat{\boldsymbol{\delta}}_y$,

$$\begin{aligned}\boldsymbol{\Xi}_\parallel\cdot\mathbf{t}+\boldsymbol{\Xi}_\perp\cdot\mathbf{t}&=\gamma_0\hat{\boldsymbol{\delta}}_y\cdot\mathbf{t},\\(2\mu_2+4\mu_4\mathbf{nn}:\mathbf{kk})(\mathbf{nn}:\mathbf{kt})&=\gamma_0\nabla_\parallel h.\end{aligned} \tag{33}$$

Integrating on both sides with respect to x gives a balance between anchoring [see Eq. (7)] and capillarity,

$$(\mu_2+\mu_4\mathbf{nn}:\mathbf{kk})(\mathbf{nn}:\mathbf{kk})=q\gamma_0 h. \tag{34}$$

Replacing $\phi=\pi/2$ in Eq. (34) we find the explicit equation for the surface relief $\tilde{h}$,

$$\tilde{h}=\frac{1}{q}(\mu_{2*}\sin^2 qx+\mu_{4*}\sin^4 qx). \tag{35}$$

Equation (35) shows the remarkable result that capillary energy $\gamma_0 qh$ is equivalent to the anchoring energy of the initial flat profile $\mu_2(\mathbf{n}\cdot\hat{\boldsymbol{\delta}}_y)^2+\mu_4(\mathbf{n}\cdot\hat{\boldsymbol{\delta}}_y)^4$ [see Eq. (1)], that is

$$\tilde{\gamma}_*-1=q\tilde{h}. \tag{36}$$

This equation allows direct calculation of all geometric and mechanical quantities of interest and shows that the energy landscape (left-hand side) is imprinted onto the surface relief landscape (right-hand side). Also we note from Eq. (36) that since anchoring coefficients are usually at most 10% of the isotropic tension, the wrinkling generated by a micron-range pitch P_0 is in the nanoscale [11,12].

2. Constrained linear shape equation model

We can also linearize Eq. (20) by assuming that the surface unit normal angle is fixed at $\phi=\pi/2$, yielding

$$\begin{aligned}\frac{\tilde{\kappa}}{2q}&=\frac{1}{2q}\frac{\tilde{F}_{\rm Dr}}{\tilde{F}_{\rm Rs}}\approx\frac{1}{2q}\frac{\tilde{F}_{\rm Dr}}{\gamma_0}\\&=\mu_{2*}\cos 2qx+2\mu_{4*}(3\sin^2 qx\cos^2 qx-\sin^4 qx).\end{aligned} \tag{37}$$

Integrating the equation twice with respect to x we find

$$\int\left(\int\tilde{\kappa}\,dx\right)dx=\tilde{h}+\text{constant}. \tag{38}$$

It can be easily verified that the surface relief we obtained from the equation above is exactly the same as that derived from Monge parametrization [Eq. (36)]. The value of this direct linearization is that reveals the exact relation between curvature κ and the director pressure $F_{\rm Dr}$ [see Eq. (20)] and

emphasize the point that wrinkling is driven by this unique capillary pressure.

3. Linear general shape equation model

Examination of the general shape Eq. (28) shows that Eq. (36) is inevitable.

If we assume that $\phi = \pi/2$, then $d\theta = -qds$ and $dx = ds$. Replacing them into Eq. (28) and letting $\gamma = \gamma_0$ on the left-hand side we have

$$-\frac{d^2}{ds^2}\left(\frac{\tilde{\gamma}}{q}\right) = -\frac{d^2}{ds^2}(\tilde{h}\gamma_0), \tag{39}$$

which implies that $\tilde{\gamma}/q = \tilde{h}\gamma_0 + C_1 s + C_2$ where C_1 and C_2 are constants. Implementing boundary condition then we verify Eq. (36), which is found to be the universal property valid for any anchoring model.

All three methods above yield the same result while they are derived from different approaches: (1) Monge parametrization emerges purely from geometry; (2) linear shape equation model is derived only by linearizing a shape ODE, an equation reflecting mechanics; and (3) the general shape equation model is an equation links mechanics and geometry. Hence, we have established that the mechanics and geometry of wrinkling in cholesteric surfaces are naturally linked.

III. WRINKLING GEOMETRY

A. Wrinkling phase diagram and symmetry relations

An important aspect of wrinkling geometry is how it reflect the symmetry properties of the linearized shape equations Eqs. (36), (38), and (39). This will help answer the questions of how the surface relief $h(x)$ profile changes when changing the handedness of the CLC or sign of P_0 and when changing the signs of the anchoring coefficients, since they are not fixed by thermodynamics. We recall that the parameters are $\mathbf{V} = [\boldsymbol{\mu}\ P_0]$. We have previously shown that the wrinkling geometry shows central symmetry in space Λ_{2n} with respect to its origin point [12]. The key idea is that for a parametric vector $\mathbf{V} \in \Lambda_{2n} \oplus \mathcal{P}$ within the linear region, surface relief can be seen as a map taking the value of vector $\boldsymbol{\mu} = [\mu_2\ \mu_4\ \mu_6\ \ldots]$ and P_0 onto an output pattern. It can be verified that $\tilde{h}$ is multilinear to $\boldsymbol{\mu}$. However, the jth term in $\tilde{h}$ is $(\mu_{2j}\sin^{2j} qx)/q$, where the wave vector q affects both magnitude as well as periodicity. Hence, the magnitude of $\tilde{h}$ as well as its statistical properties scaled by P_0 such as mean value or standard deviation are linear to all the inputs.

A direct application of this result is the surface profile symmetry relations:

$$\begin{aligned}\frac{\tilde{\gamma}_*(\boldsymbol{\mu}, P_0) - 1}{q} &= \tilde{h}(\boldsymbol{\mu}, P_0) = \tilde{h}(-\boldsymbol{\mu}, -P_0) \\ &= -\tilde{h}(-\boldsymbol{\mu}, P_0) = -\tilde{h}(\boldsymbol{\mu}, -P_0).\end{aligned}$$

For example, changing the signs of all anchoring coefficients and pitch will leave the surface profile intact. However, a pitch inversion will reverse the profile. This could be important in applications when controlling the flatness or peak sharpness present in $h(x)$ is important. Changing the sign of cholesteric pitch P_0 only results in a mirror reflection

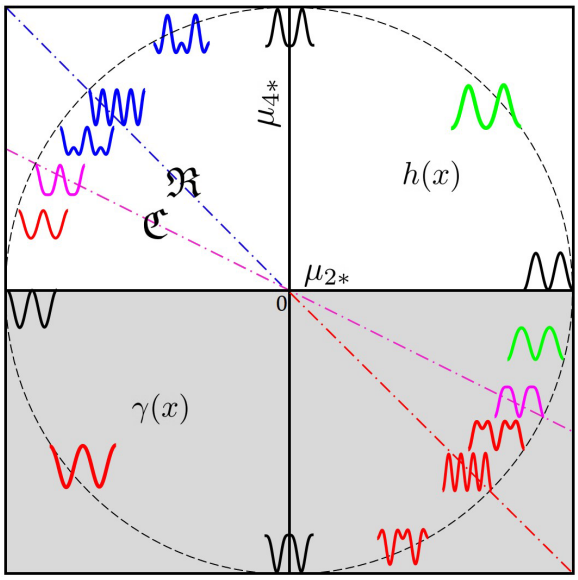

FIG. 3. Wrinkling phase diagram as a function of anchoring coefficients. The top semicircle shows the surface profile $h(x)$ and the bottom semicircle shows the surface tension profiles $\gamma(x)$. The resonance line $\mathfrak{R}$ is $\mu_{2*} + \mu_{4*} = 0$ and the critical line $\mathfrak{C}$ is $\mu_{2*} + 2\mu_{4*} = 0$ (see text). At the resonance line $\mathfrak{R}$ the quartic and quadratic harmonics is a maximum. The sectors within the $\mathfrak{C}$ and μ_{4*} lines display two waves, and the rest of the sectors only one wave. According to Eq. (36) the surface tension γ is proportional to the surface relief $h(x)$ and hence essentially the same; thus we show $h(x)$ on the top semicircle and γ on the bottom semi-circle. The symmetry of the $h(x)$ profiles (or the γ profiles) follow the graphical equations in Sec. III A.

and will not cause any phase shift. The phase shift is only dependent on the ratio μ_2/μ_4, and is independent of the helicity P_0. Next we evaluate the surface roughness behavior as a function of anchoring coefficients; whenever tractable we present general results for $\boldsymbol{\mu} = [\mu_2\ \mu_4\ \mu_6 \ldots]$ but for specificity we concentrate on the quartic anchoring model $\boldsymbol{\mu} = [\mu_2\ \mu_4]$. Figure 3 shows the wrinkling phase diagram for the quartic model in terms of the two anchoring coefficients. The figure shows the patterns of surface relief profile (upper plane) and energy profile (lower plane with gray shading area) when fixing P_0 as a constant. The circle is $\mu_{2*}^2 + \mu_{4*}^4 = C^2$ where $C \in \mathbb{R}^+$. The resonance line $\mathfrak{R}$ is $\mu_{2*} + \mu_{4*} = 0$ and the critical line C is $\mathfrak{C}$ is $\mu_{2*} + 2\mu_{4*} = 0$. Figure 3 verifies the correspondence between $h(x)$ and $\gamma(x)$ [see Eq. (36)], as well as the central symmetry shown in the Λ_4 space. The colors in Fig. 3 serve to categorize different regions in Λ_4 where we adapted from previous discussion [12]. The anchoring space is divided into 6 sectors according to the emergence of double wrinkling or single wrinkling, by the vertical $\mu_2 = 0$ line, the oblique resonance line $\mathfrak{R}$, and the oblique critical line $\mathfrak{C}$. Double wrinkling occurs in (a) the first sector of the second quadrant (i.e., between the vertical $\mu_2 = 0$ line and the oblique critical line $\mathfrak{C}$; blue profiles), and in (b) the first sector of the fourth quadrant (i.e., between the vertical $\mu_2 = 0$ line and the oblique $\mathfrak{C}$ critical line; red profiles). In terms of signs $(+-)$ of the anchoring coefficients, double wrinkling only occurs in the $(-+)$ and $(+-)$ sectors of the phase diagram in

TABLE I. Statistics of surface geometry.

Parameter	Symbols	Definition	Description
Mean	m	$M[1,0]$	Average value of $h(x)$
Arithmetic Mean	Ra	$M\|1,m\|$[a]	Average deviation with absolute value accumulated
Variance	σ^2	$M[2,m]$	Deviation of $h(x)$ with respect to m
Skewness	Rsk	$M[3,m]/\sigma^3$	Measure of the asymmetry
Kurtosis	Rku	$M[4,m]/\sigma^4$	Measure of the tailedness

[a]Defined as $\frac{1}{P_0}\int_0^{P_0}|h(x)-m|\,dx$, where the square bracket in Eq. (42) is replaced with an absolute value.

Fig. 3. Hence, richer double wrinkling is relatively abundant in the anchoring space. Also note that the resonance line $\mathfrak{R}$ denotes maximal interaction between the harmonics and results in single wrinkling. Figure 3 also indicates that in the $(-+)$ mode peaks are up and valleys are down, while in the $(+-)$ mode the reverse is true. This important effect is captured by the third moment of the surface height distribution (skewness) discussed below. An inversion $h \to -h$ results an inversion of the surface profile while maintaining the space above as air and the space below as liquid crystal. Finally, we see that that signed ratio of the anchoring coefficients is the main variable controlling wrinkling while Eq. (35) indicates that $\boldsymbol{\mu}$ controls the amplitude only. An important close similarity is the shape and curvedness of surfaces [42] with the former given by a curvature ratio, and the latter by the sum of curvature squares. The preferred tilt angle is related to the ratio of anchoring coefficients $\theta_s = \arccos\sqrt{-r}$ $[r = \mu_2/(2\mu_4)]$, corresponding to a local minimum in the energy profile $\partial_\theta \gamma|_{\theta_s} = 0$. It also implies that there are no complicated wrinkling patterns on the first and third quadrants as they do in the second and fourth quadrants in Fig. 3, since $\sqrt{-r}$ is not defined for $r > 0$ and $\partial_\theta \gamma = 0$ gives trivial solution.

B. Moments characterization of surface geometry

A detailed characterization of surface geometry requires specification of the moments of the surface relief $M[n,m]$ with respect to the mean m. We note that the common base line of the surface relief is fixed and defined by the given director filed at $s = 0$ $(\mathbf{n} = \hat{\boldsymbol{\delta}}_x)$ and is equal to $h(s=0) = 0$ for all cases. We start with the quantities that appear in calculating the moments that characterize wrinkling. The Mclaurin series of $(1-x)^{-1/2}$ is

$$\frac{1}{\sqrt{1-x}} = \sum_{n=0}^{\infty}\frac{(2n-1)!!}{2^n n!}x^n = \sum_{n=0}^{\infty}\frac{1}{\sqrt{\pi}}\frac{\Gamma(n+\frac{1}{2})}{\Gamma(n+1)}x^n, \quad (40)$$

where Γ is the gamma function. Let the nth coefficient of x^n be $\mathfrak{b}_n$, and denote dimensionless series $\{\mathfrak{b}_n\}$. Most common values are $\mathfrak{b}_1 = 1/2$, $\mathfrak{b}_2 = 3/8$, $\mathfrak{b}_3 = 5/16$, and $\mathfrak{b}_4 = 35/128$. Next we establish the important relation of the $\mathfrak{b}_n$ to sine integrals that appear when integrating h and its powers (i.e., computing the moments). In the following computations, we always assume $P_0 = 1\mu$m unless otherwise stated. We find that the nth (n is even) moment of $\sin qx$ satisfies the following identity (consult Appendix C):

$$\int_0^{P_0}\sin^n(qx)\,dx = P_0\mathfrak{b}_{n/2}. \quad (41)$$

The statistical parameters to describe surface profile are summarized to Table I, where we use standard notation [22]. In Table I, we define $M[n,m]$ as the nth moment of $h(x)-m$ in Λ_4 computed by (see Appendix C)

$$M[n,m] := \frac{1}{P_0}\int_0^{P_0}[h(x)-m]^n\,dx \doteq \sum_{i=0}^{n}\binom{n}{i}(-\tilde{m})^{n-i}\sum_{j=0}^{i}\binom{i}{j}\mu_{2*}^{j}\mu_{4*}^{i-j}\mathfrak{b}_{2i-j}. \quad (42)$$

This formula reveals the central role $\mathfrak{b}_n$ and also the signs of the anchoring coefficients for odd moments that control up-to-down h-profile features.

1. Mean and deviation

The mean m represents average line and σ^2 captures the deviation of surface from the mean value. Both σ and Ra describe the deviation from average line (see Table I). In Eq. (24) we dropped the constant while integrating, which defined automatically the straight line parallel to the x axis and passing through the point p where director field $\mathbf{n}_p = [1 \quad 0]^\intercal$ as the baseline (from the boundary condition we defined). Then m is an invariant and is irrelevant to how the surface is characterized. Using linear theory, in quartic model $\tilde{m}$ becomes

$$\tilde{m} = \frac{1}{q}(\mathfrak{b}_1\mu_{2*} + \mathfrak{b}_2\mu_{4*}), \quad (43)$$

while $\tilde{\sigma}$ reduces to

$$\tilde{\sigma}^2 = \frac{1}{q^2}\big[(\mathfrak{b}_2 - \mathfrak{b}_1^2)\mu_{2*}^2 + 2(\mathfrak{b}_3 - \mathfrak{b}_1\mathfrak{b}_2)\mu_{2*}\mu_{4*} + (\mathfrak{b}_4 - \mathfrak{b}_2^2)\mu_{4*}^2\big]. \quad (44)$$

Figure 4 shows the numerical solutions (colors correspond to numerical values given in the side bar) of the mean m and arithmetic mean Ra in the parametric plane, obtained from Eqs. (20), (24), and (42). We can observe that the mean value almost vanishes along the resonance line $\mathfrak{R}$. In addition, due to the symmetry of Λ_4, any two points symmetric with respect to the origin should have the same magnitude but opposite sign of m. For the arithmetic mean Ra, the minimum value occurs along $\mathfrak{R}$, and closer to the origin of Λ_4, a darker color appears in the Ra plot, which corresponds to the fact that weak anchoring gives weak deviation. An important technical application of Ra is to categorize roughness with a grade number N since a high Ra implies a very rough surface. Grade number $N1$ correspond to a $0.025\,\mu$m roughness and $N4$ to $0.2\,\mu$m [22,43]. Roughness grade numbers $N1$ to $N4$, in our

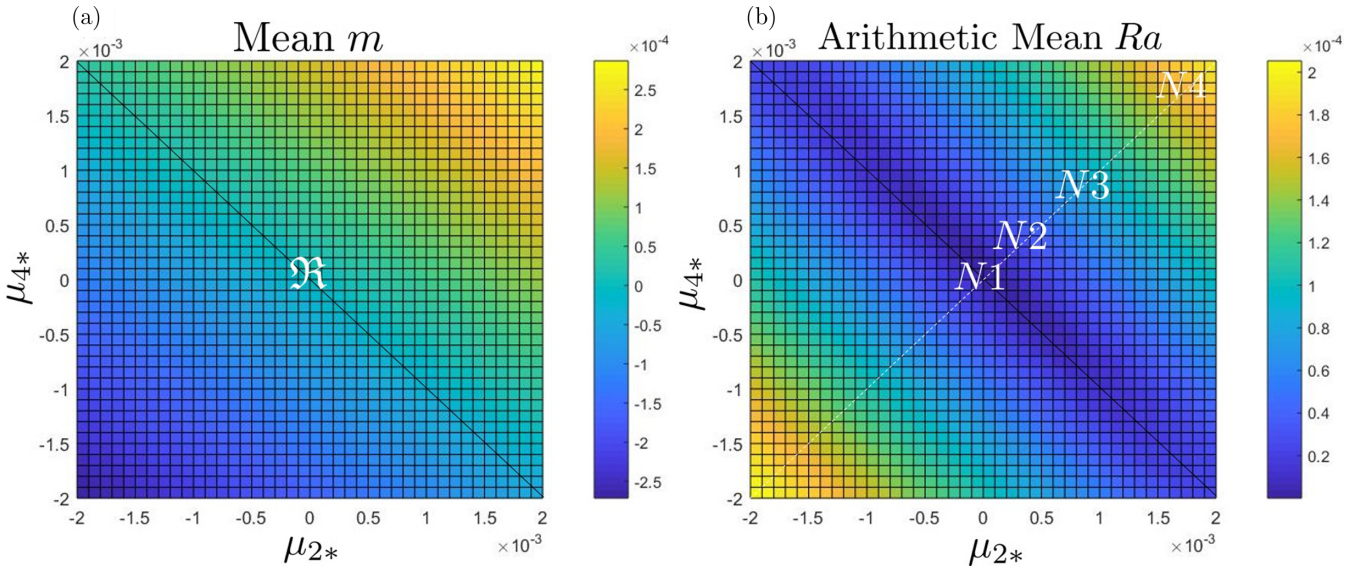

FIG. 4. Mean value m (a) and arithmetic mean Ra (b) as a function of two dimensionless anchoring coefficients. See Table I and Appendix C for definitions and details. The following discussion refers to Fig. 5, where we fix the magnitude of $\boldsymbol{\mu}$ as a constant to discuss the contributions of μ_2 and μ_4 to the statistical properties of the surface. The mean vanishes close to the resonance line and the maximum is along a line normal to this line. The arithmetic mean is a minimum along the resonance line and increases normal to this line. The labels $N1$–$N4$ denote characteristic roughness values used to characterize rough surfaces, with $N1$ having low and $N4$ high roughness. The location of $N1$–$N4$ in the anchoring diagram shows the practical applicability of anchoring.

soft matter material, are shown in Fig. 4(b) by assuming the scale of the magnitude of $P_0\mu_{2*}$ is 1mm. We can see that surface roughness grade number is distributed perpendicular to $\mathfrak{R}$; since $N1$ corresponds to 0.025 μm and $N4$ to 0.2 μm we see that anchoring is compatible with industrial roughness values for reasonable pitch P_0 scales [22].

We can shed more light into the specific trends shown in Fig. 4 by analyzing Eq. (42) in conjunction with the wrinkling geometry of the anchoring phase diagram (Fig. 3). According to Eq. (43) The mean value m can be set to zero by forcing $\mathfrak{b}_1\mu_{2*} = -\mathfrak{b}_2\mu_{4*}$, while according to Eq. (44) the standard deviation σ can be arbitrarily close to zero, which corresponds to a flat surface. Hence, we choose two parameters along a closed circle (see Fig. 5): $\mu_{2*}^2 + \mu_{4*}^2 = C^2$. We seek to find the extreme values of mean and deviation along this characteristic circle. Figure 4 shows that the line along which m vanishes is perpendicular to the line where m reaches extremum. Also the line along which σ reaches maximum is a mirror symmetry of the line where σ reaches a minimum with respect to μ_{4*}/C line.

Since $\mathfrak{b}_j = \mathfrak{b}_{j-1}(1 - \frac{1}{2j})$, so $\mathfrak{b}_j$ contributes less and less as j increases. The monotonic decrease of series $\{\mathfrak{b}_n\}$ is the reason why $m = 0$ requires $|\mu_4| > |\mu_2|$. The numerical solution given by Fig. 4 (see color intensity grading and Ni labels) matches our discussion that m essentially vanishes along $\mathfrak{R}$. This important results establishes that the maxima in m corresponds to a $(++)$ mode and the maxima in σ to a $(++)$ and $(--)$ modes.

As expected, we can generalize the extrema characterization to higher-order Λ_{2n} anchoring models. Consider a special but realistic condition when each anchoring coefficient μ_{2i} is proportional to $\mathfrak{b}_i$ such that $\mu_{2i*} = \alpha\mathfrak{b}_i$ (α is a nonzero constant); as noted below Eq. (44) the coefficients decrease with "i," and hence we are assuming that the anchoring coefficients also decrease with "i." Then $\tilde{m} = \alpha S/q$, where $S = \sum_{i=1}^{n} \mathfrak{b}_i^2$ and anchoring coefficients are restricted on an

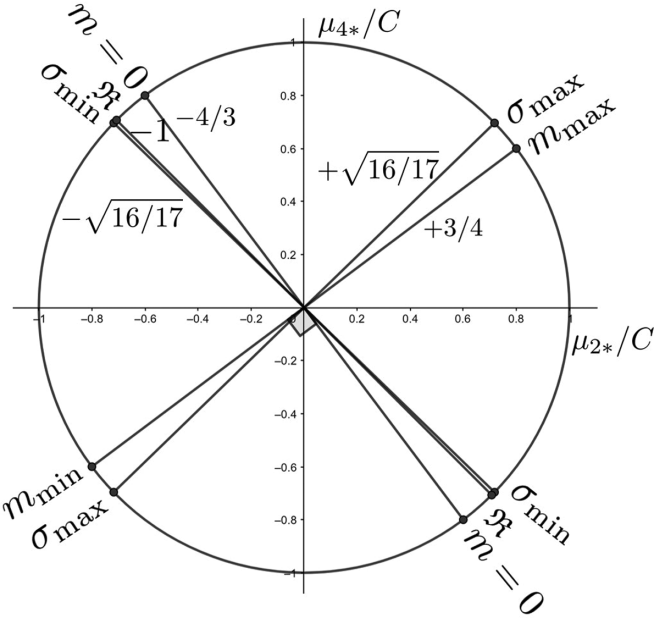

FIG. 5. Extremum values distribution for m and σ restricted by $\mu_{2*}^2 + \mu_{4*}^2 = C^2$ within Λ_4 space, with number next to each line representing its slope. The mini-max lines crisscrossing the anchoring phase diagram show the versatility of anchoring as a wrinkling force. The radial lines also show that essential wrinkling qualities depend on the ratio of the anchoring coefficients (azimuthal angle in this diagram) and not on C (sum of anchoring amplitudes square or radial direction in this diagram).

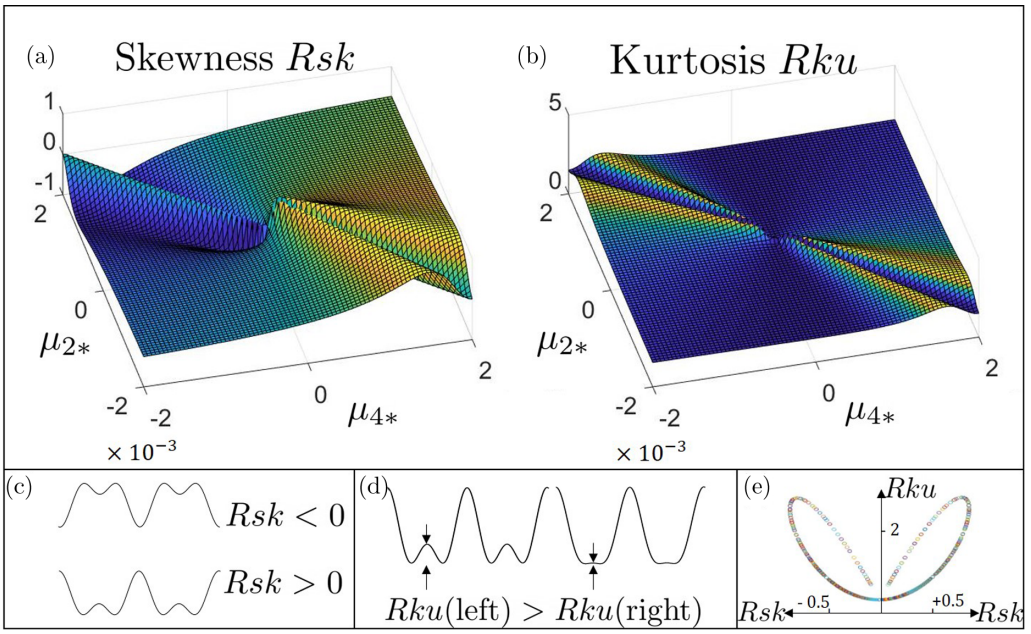

FIG. 6. Computed skewness Rsk (a) and kurtosis Rku (b) surfaces as a function of the two anchoring coefficients. Representative surface profiles with different skewness (c) and kurtosis (d). Skewness as a function of kurtosis (e), as the anchoring coefficients change, showing mirror symmetry.

n sphere $\sum_{i=1}^{n} \mu_{2i*}^2 = C^2$ where C is a positive constant. It can be verified that this special condition is exactly the solution giving the extremum $\tilde{m}$. And the constant can be computed by $\alpha = -C/\sqrt{S}$ (proof is given by Appendix D). The Borsuk-Ulam [44] theorem requires that a vanishing m must exist, corresponding to an $(n-1)$ dimensional hyperplane $\sum_{i=1}^{n} \mathfrak{b}_i \mu_{2i} = 0$, which is perpendicular to the line represented by this special condition. This important result indicates vanishing m for any anchoring order model. We note that since the director field is fixed at $\mathbf{n}(x=0) = \hat{\boldsymbol{\delta}}_x$, the zero mean can not be shifted away.

2. *Skewness and kurtosis*

The third-order moment, normalized skewness Rsk quantifies the asymmetry of the surface profile, while the fourth-order moment, normalized kurtosis Rku intuitively describes the thickness of the tail of the surface profile distribution. Figure 6 shows the numerical computations using Eqs. (20), (24), and (42) with $P_0 = 1\ \mu$m. The geometric meaning of Rsk is given by the h profiles in Fig. 6(c). The positive or negative sign of Rsk represents two asymmetric patterns shown in the figure, where positive skewness indicates a surface with tall peaks and negative skewness indicates a surface with deep valleys. The magnitude of Rsk measures the magnitude of this asymmetry. Figure 6(a) shows that Rsk vanishes along $\mathfrak{R}$, and almost vanishes in the first quadrant and third quadrant. We can observe that Rsk > 0 in the second quadrant and Rsk < 0 in the fourth quadrant of Λ_4.

Figure 6(b) shows the kurtosis surface with intersecting double folds, converging along $\mathfrak{R}$. We can also observe that Rku $\neq 0$ except at $\boldsymbol{\mu} = \mathbf{0}$, where the surface is flat. In Fig. 6(d), we can see that the geometric meaning of Rku is how much the small tails contribute to the total wave pattern. Rku reaches its minimum along $\mathfrak{R}$, also in the first and third quadrant.

This can be explained since wrinkling waves are identical along $\mathfrak{R}$ and show no difference in the first and third quadrant. Rku displays rotational symmetry in the second and fourth quadrant, hence we only need to analyze the second quadrant. Small tails contribute the most when the surface relief occur in the vicinity of $\mathfrak{R}$ but not exactly along $\mathfrak{R}$. The essential features of the intersecting double folds are as follows. Therefore, if we track Rku along a 1/4 circle parametrized by $\mu_{2*}^2 + \mu_{4*}^2 = C^2$ where C is a positive constant from $\mu_{2*} = -C$ to $\mu_{2*} = 0$, then we should expect Rku to increase initially due to the emergence of small tails, then decreases until the circle reaches $\mu_{2*} = -\sqrt{2}C/2$ since waves are identical along $\mathfrak{R}$, exhibiting a local minimum in kurtosis. If we then continue to move along the 1/4 circle until reaching $\mu_{2*} = 0$ from $\mathfrak{R}$, then the process is reversed and we find an increasing and then decreasing Rku. Considering now the Rsk plot [Fig. 6(a)], we find that the magnitude of Rsk shows the same trends as that of Rku. These insights reveal that the vicinity of the resonance line exhibit higher magnitudes in kurtosis and skewness which affect functionalities such as friction.

Kurtosis Rku as a function of skewness Rsk is shown in Fig. 6(e). The symmetric petal pattern corresponds to a bifolium [45], another classical planar curve associated with biological forms. The importance of this plot is that it reveals the versatility of anchoring-driven wrinkling. Using hard materials and respective processes only specific areas of the kurtosis-skewness plane are achievable [46].

Kurtosis is always below 3 (so-called Gaussian profile), indicating a gradually changing surface curvature. The petal pattern is an intrinsic plot, and it does not depend on $\boldsymbol{\mu}$ or P_0. Given a certain $\boldsymbol{\mu}$ and P_0, we can locate a point in Rsk-Rku plot. Points are denser around the bottom point

shown in Fig. 6, implying that most of the points in Λ_4 are surrounding the minimum Rsk (or Rku), corresponding to the fact that most regions in Λ_4 yield a one-wavelength pattern (two waves within one period). As for the applications, the Rsk-Rku plot plays an important role in surface science and industry. For example, it is possible to lower static friction coefficients by increasing high Rku while remaining positive Rsk [47]. Rsk-Rku plot is also used to measure the roughness of biological surface topography [48].

IV. WRINKLING MECHANICS

In this section, we characterize wrinkling mechanics using the capillary pressure and the capillary vector $\boldsymbol{\Xi}$. It will be shown that the mechanical information content in the capillary pressures can be expressed in polar coordinates and that the stress state can be quantized by winding numbers W_p of generalized Lamé stress curves, which is an intuitive method to complement the Mohr's circle in mechanical analysis defined by $\sum_i T_i^2/\sigma_i^2 = 1$, where T_i is the stress vector and σ_i the stress.

A. Capillary pressure

The mechanics behind surface wrinkling is the cancellation between dilation pressure, rotation pressure and director pressure, as shown in Eq. (19). These pressures play different roles in surface wrinkling and are expressed by

$$\begin{aligned} P_{\text{dil}} &= -\kappa[1+\mu_{2*}(\mathbf{nn}:\mathbf{kk})+\mu_{4*}(\mathbf{nn}:\mathbf{kk})^2], \\ P_{\text{rot}} &= -\kappa[2\mu_{2*}(\mathbf{nn}:\mathbf{tt}-\mathbf{nn}:\mathbf{kk}) \\ &\quad +4\mu_{4*}(\mathbf{nn}:\mathbf{kk})(3\mathbf{nn}:\mathbf{tt}-\mathbf{nn}:\mathbf{kk})], \\ P_{\text{dir}} &= 2[\mu_{2*}+2\mu_{4*}(\mathbf{nn}:\mathbf{kk})]\left(\mathbf{n}\otimes\frac{\partial\mathbf{n}}{\partial s}:\mathbf{tk}\right) \\ &\quad +2[\mu_{2*}+6\mu_{4*}(\mathbf{nn}:\mathbf{kk})]\left(\mathbf{n}\otimes\frac{\partial\mathbf{n}}{\partial s}:\mathbf{kt}\right). \end{aligned} \tag{45}$$

The dilation pressure P_{dil} represents the area dilation effect, which is related to the expansion or shrinkage of surface area (Laplace pressure). The rotation pressure P_{rot} represents a small rotation of surface area, whose contribution to the surface wrinkling is brought by tangential component $\boldsymbol{\Xi}_{\parallel}$ (also known as Herring's pressure). They are two pressures related to the surface hence they both have an explicit κ term in their equations. The director pressure P_{dir} is introduced by director surface gradients, so it does not contain direct geometric curvature information. As mentioned above, the director pressure is the driving force that causes wrinkling patterns in this model.

Figure 7 shows polar plots P_{dil}, P_{dir}, and P_{rot} as a function of the relative angle between the unit normal and the director $\theta = \phi - qx$. P_{dil} and P_{dir} dominate the magnitude, and P_{rot} is the small difference between them. The reason is that dilation effect is to the first order proportional to the curvature κ times γ_0; while the rotation effect under small wrinkling conditions is proportional to κ times γ_{an} and since $\gamma_0 \gg \gamma_{\text{an}}$, $P_{\text{dil}} \gg P_{\text{rot}}$. Hence, $P_{\text{dil}} \approx -P_{\text{dir}}$ if we neglect rotation pressure, which implies that dilation pressure and director pressure are always out-of-phase. Another important identity is that the direction

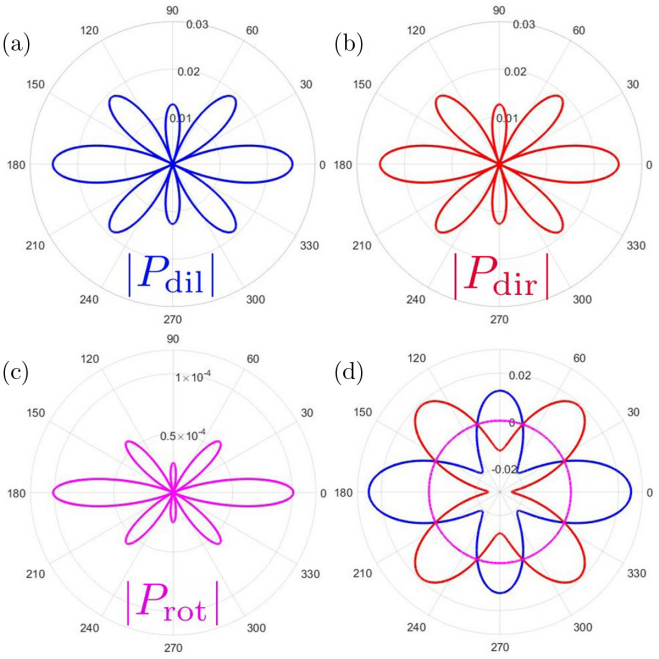

FIG. 7. Capillary pressures visualized in polar plot where rotation angle $\theta = \phi - qx$. Blue, red, and magenta paths represent dilation (a), director (b), and rotation (c) pressures, respectively. ($\mu_{2*} = -0.002$ and $\mu_{4*} = +0.0015$). (d) Shows the three pressures (here we compute the real value instead of absolute value) in a single polar coordinate system where 0 is the ring close to the magenta curve. It also shows how the total capillary pressure vanishes [Eq. (19)].

of rotation pressure is only dependent to the direction of helix pitch, i.e., $\text{sgn}(P_{\text{rot}}) = -\text{sgn}(P_0)$. This relation can be found by Eq. (53).

B. Capillary vector and complex plane curve

1. Complex capillary vector $\boldsymbol{\beta}$

Figure 1 and Eq. (18) show that stresses and the capillary vector are related by a simple $\pi/2$ rotation, suggesting the usefulness of using complex analysis, as done here. According to Eq. (17) (consult Appendix B) the eigenvalues of the surface stress tensor are $\Xi_{\perp}$ and $-\Xi_{\parallel}$. The three tensor invariants are

$$\begin{aligned} I_1 &= \text{tr}\mathbf{T}_s = \Xi_{\perp} - \Xi_{\parallel}, \\ I_2 &= \tfrac{1}{2}\left[(\text{tr}\mathbf{T}_s)^2 - \left(\text{tr}\mathbf{T}_s^2\right)\right] = -\Xi_{\perp}\Xi_{\parallel}, \\ I_3 &= \det\mathbf{T}_s = I_2. \end{aligned} \tag{46}$$

Equation (46) implies that any scalar function depending on capillary vectors is independent from rotations of the coordinate system. Define a dimensionless complex capillary number β as

$$\beta = \Xi_{\parallel *} + \Xi_{\perp *} i. \tag{47}$$

As we show below, β is the core concept whose topology serves as the bridge between geometry and mechanics. If we are moving toward the positive x direction along the arc-length s, then $\boldsymbol{\Xi}_{\parallel}$ stays in the tangent space. This is the reason why we assign $\boldsymbol{\Xi}_{\parallel}$ to the real part of β. The complex capillary

number also has a matrix form **B**,

$$\mathbf{B} = \Xi_{\parallel *}\mathbf{I} + \Xi_{\perp *}\mathbf{R}, \tag{48}$$

where **I** is the identity matrix and **R** is the rotation matrix that appears in Eq. (18). The diagonalization of **B** contains its complex conjugate

$$\mathrm{Diag}\mathbf{B} = \begin{bmatrix} \bar{\beta} & 0 \\ 0 & \beta \end{bmatrix}. \tag{49}$$

We can easily link β, **B**, Ξ, and $\mathbf{T}_s$ by

$$\mathbf{B}\mathbf{B}^{\dagger} = \beta\bar{\beta}\mathbf{I} = \Xi^2\mathbf{I} = \left(\mathrm{tr}\mathbf{T}_s^2\right)\mathbf{I}. \tag{50}$$

Hence, the ratio $\mathbf{B}/\Xi$ is a special unitary matrix$\in$ SU(2), while in Eq. (48), both **I** and **R** are special orthogonal matrices $\in$SO(2). Later we will show that **B** provides the same information as the mechanogeometry transformation matrix **Y** introduced in Sec. V B 3, that transforms the geometric frame $(\mathbf{t}, \mathbf{k})$ into the mechanical frame $(\boldsymbol{\Xi}, \mathbf{T}_v)$, shown in Fig. 1.

According to classical mechanics of 2D surfaces with 2D stress components, the typical Lamé stress curve is an elliptical closed curve [26]. In our model with 2D stresses we will show that the elliptical Lamé stress curves of classical mechanics may become Limaçon (cardioidlike) curves [45] according to the degree of surface wrinkling. For example, for a quartic anchoring model, plotting for an anchoring condition along the resonance curve gives an ellipse, but plotting these quantities for a condition of double wrinkling produces a closes curve with an intersection (see middle row of Fig. 11). Here we wish to establish a classification scheme based on winding number W_p for these generalized Lamé stress curves that provides a direct connection with geometry.

To first show the genesis of Limaçon stress curves, we consider a special simple case of a quartic model with $\mu_2 = 0$, and the Lamé stress curve obtained by observation is

$$\left[\frac{\Xi_{\parallel}^2}{\mu_4^2} + \frac{16(\Xi_{\perp} - \gamma_0)^2}{\mu_4^2}\right]^2 = 4\left[\frac{4(\Xi_{\perp} - \gamma_0)}{\mu_4}\right]^3, \tag{51}$$

which is an equation consistent with a Limaçon curve [45] and that we can compute numerically by using Eqs. (6), (7), and (20) for arbitrary anchoring constants.

Since β represents a Limaçon stress curve in the complex plane it has a winding number W_p. The winding number W_p of a stress loop C with respect to a point p in the complex plane $\mathbb{C}^1$ is defined as

$$W_p = \frac{1}{2\pi i}\oint_C \frac{1}{z - p}dz, \tag{52}$$

whose geometric meaning is the number of net loops around a point. This number can help us to identify the total waves of $h(x)$ within one period. W_p varies according to the position of p. We use W_p to refer to the possible maximum W_p a loop can have due to the variation of W_p.

In general, β describes s a closed loop pattern with a certain winding number in parametric space Λ_{2n}. The more nonvanishing anchoring coefficients there are, the more complicated pattern β exhibits. Particularly, β degenerates to a simple Lamé's stress ellipse in Λ_2 space.

The Limaçon curve defines the stress states as the surface wrinkles. Importantly, when the surface profile changes slope $(+-)$ or $(-+)$ the bending stress [Eq. (17)] or real component of β vanishes. The Limaçon curve β shows that in Λ_4 has three critical points where $\frac{d\mathrm{Re}\beta}{d\mathrm{Im}\beta} = 0$, and they are summarized by Table II. Table II shows that zero bending stress corresponds to different normal (extensional) stresses, creating complex stress conditions along the surface.

TABLE II. Three points where $\Xi_{\parallel} = 0$ (or bending stress).

No.	Reβ	Imβ
1	0	1
2	0	$1 + \mu_{2*} + \mu_{4*}$
3	0	$1 - r\mu_{2*} + r^2\mu_{4*}$[a]

[a] r is the anchoring ratio defined by $\frac{\mu_2}{2\mu_4}$.

Figure 8 shows the maximum winding number as a function of the anchoring model order. The maximum winding number W_p is linearly related to the highest anchoring term in Eq. (1). β is expected to have a maximum winding number of n, and minimum winding number of 1 in Λ_{2n} space (neglect flat surface condition). For example, for $n = 2$, $W_p = 1$ has a simple stress ellipse with two bending stress extrema, while for $W_p = 2$, the extrema are shown in Table II. In partial summary, in contrast to plotting pressure and stress spatial profiles, we condensed all mechanical information in polar pressure plots (Fig. 7) and in quantized winding numbers of stress curves as functions of only the anchoring order model (Fig. 8).

β does not admit a classical feature since σ_i is not a constant, which changes from point to point. So $T_1^2/\sigma_1^2 + T_2^2/\sigma_2^2 = 1$ in the frame $\{T_1, T_2\}$ is actually not an ellipse. This feature is unique to the anchoring-generated surface stresses and hence the simple ellipse of classical materials becomes closed planar curves sometimes with intersections.

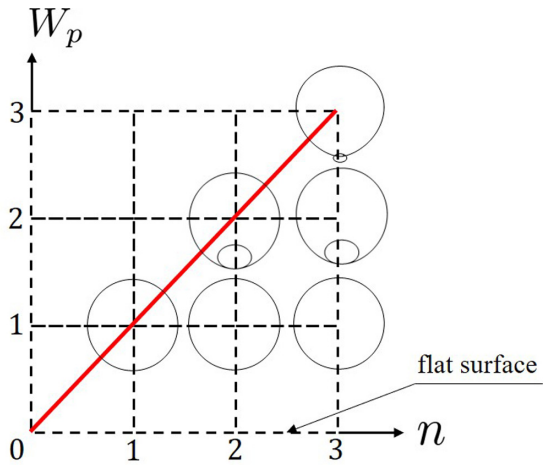

FIG. 8. Maximum winding number W_p as a function of the highest anchoring model order n and Limaçon curves. $W_p = 0$ represents a single point in β plot and further a flat surface. All the possible patterns are limited between a flat surface and red line. For example, for the quartic model, the possible winding numbers of the stress loops are 1 and 2, which corresponds to single and double wrinkling in Fig. 3.

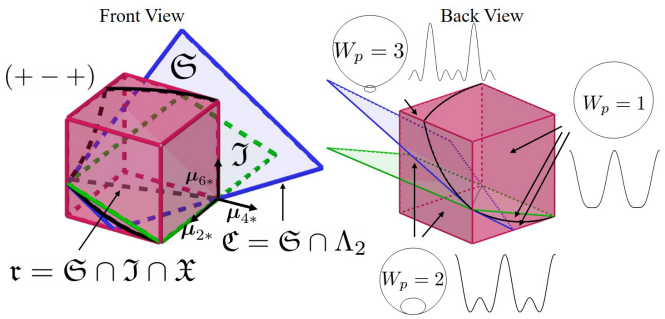

FIG. 9. High winding number stress loops in the anchoring space for the sextic anchoring model ($n = 3$). Front view and back view of a subspace $(+-+)$ within Λ_6 where $W_p = 3$ is possible; the signs corresponds to the three anchoring coefficients of the $n = 3$ model. $W_p = 3$ can only be found in the region sandwiched in the middle of $\mathfrak{S}$ and $\mathfrak{X}$. The Limaçon stress curves for $W_p = 1, 2, 3$ are shown on the right back view figure. The figure was computed using the intersections of $\mathfrak{S}$, $\mathfrak{J}$, and $\mathfrak{X}$ (see text and Appendix E).

2. Winding number landscapes in higher-order models

Here we generalize winding number results for $n = 3$. From Fig. 8, it is possible to have $W_p = 2$ in Λ_4 and $W_p = 3$ in Λ_6. If we write $\boldsymbol{\mu} = [\mu_2\ \mu_4\ \mu_6]$, then the components of $\boldsymbol{\mu}$ span a 3D space, which is the parametric space Λ_6. For simplicity, we use an ordered triplet $(\pm\pm\pm)$ to represent the sign of each anchoring coefficient. We found that only $(+-+)$ and $(-+-)$ quadrants allow us to have $W_p = 3$. Λ_6 also shows central symmetry, so we only need to evaluate the $(+-+)$ quadrant, shown in Fig. 9, together with the relevant planes quoted below.

The following surfaces serve as characteristic surfaces such that they are the boundaries to categorize different wrinkling regions of Λ_6:

$$\begin{aligned} \mathfrak{X} &: \mu_4^2 = 3\mu_2\mu_6, \\ \mathfrak{J} &: -3\mu_6 = \mu_4, \\ \mathfrak{S} &: -3\mu_6 = \mu_2 + 2\mu_4. \end{aligned}$$

In Fig. 9, only the region between $\mathfrak{S}$ and $\mathfrak{X}$ allows $W_p = 3$. We can observe from Fig. 9 that in the region where $W_p = 3$, there exists one loop that is way more bigger than the other two. That loop is so big such that it is impossible to adjust μ to force three loops overlap. This phenomenon actually implies that we can never get 6 identical waves within one period in Λ_6. The details of this derivation are in Appendix E. This important result on generalized models shows that higher harmonics can at most create only hierarchical effects, such as small ripples on larger scales wrinkling.

In summary, from the property of cholesteric liquid crystals and shape equation, we can expect a periodic structure shown in the surface profile. If we have a point at position x, then we should expect that the point at $x + P_0$ should have the same mechanical behavior. This is why β is a closed curve. A closed curve provides the opportunity to measure how many "loops" there are. The "loops" are the nontrivial information given by the curve. It shows that from x to $x + P_0$, a number of "detours" are taken. The "detours" represent the wrinkling patterns. From an elasticity point of view, the wrinkling patterns decrease the total energy.

V. MECHANOGEOMETRY OF WRINKLING

In this section we synthesize the relationships between mechanics (capillary pressures, capillary vectors, winding numbers) and geometry (surface relief, curvature) using methods that lead to scaling relations and invariant that indicates surface property.

A. Capillary pressures-geometry relation

We find that linearized capillary pressures [see Eq. (45)] are dependent on curvature according to the following relations:

$$\tilde{P}_{\text{dil}} = -\tilde{\kappa}, \quad \tilde{P}_{\text{rot}} = -\frac{\tilde{\kappa}^2}{q}, \quad \text{and} \quad \tilde{P}_{\text{dir}} = \tilde{\kappa} + \frac{\tilde{\kappa}^2}{q}. \tag{53}$$

If we plot the three capillary pressures as a function of curvature, then Eq. (53) indicates that there exist three parameter-free universal curves. In each plot, μ_2 and μ_4 only affect the arc-length of these curves (starting and end points). Only the arc-length of P_{dil}-κ curve is linear while the others are not. Generally, the span of curvature is dependent to anchoring coefficients, and ideally linear to $1/P_0$. This finding has an intuitive explanation. Consider the situation where P_0 is doubled while maintaining the same anchoring condition, the span of curvature should reduce to half. A numerical validation and details of discussion of Eq. (53) are given by previous work [12]. Equation (53) encapsulates the symmetry relations shown in Sec. III A. If we change the sign of the chirality (q), then the only way to accommodate this change is through a mirror symmetry along the x axis. As mentioned above, chiral dopants control surface relief features such as skewness.

From Fig. 7, we can observe that winding number W_p and the absolute value of dilation pressure $|P_{\text{dil}}|$ are linked by: number of petal lobes $= 4 \times W_p$. This relation can be easily found through $P_{\text{dil}} = \kappa\gamma$.

B. Capillary vectors-geometry relation

The wrinkling geometry and wrinkling mechanics are strongly connected. To reveal that link, we will first give a detailed explanation of how mechanics and geometry are linked for a special nontrivial condition where we only have one nonvanishing anchoring coefficient μ_2. Then we generalize the conclusion to n nonvanishing anchoring coefficients' model. In the end of this subsection, a mechanogeometry transformation matrix will serve as a summary to the mechanogeometry relation.

1. Special condition: Quartic model with $\mu_4 = 0$

If $\mu_4 = 0$ in the quartic model, then we obtain the quadratic model and the surface pattern is a single-wavelength sinusoidal profile (see Fig. 3). The director pressure expression [Eq. (45)] is a contraction of symmetric tensors:

$$P_{\text{dir}} = \mu_{2*}\left(\mathbf{n} \otimes \frac{\partial \mathbf{n}}{\partial s} + \frac{\partial \mathbf{n}}{\partial s} \otimes \mathbf{n}\right) : (\mathbf{tk} + \mathbf{kt}). \tag{54}$$

Equation (54) indicates that the driving force is symmetric, hence a symmetric structure with vanishing skewness, Rsk = 0 should be generated. Under this condition, β degenerates to a Lamé ellipse and satisfies

$$\left(\frac{\mathrm{Im}\beta - \mathcal{C}_0}{\frac{1}{2}\mu_{2*}}\right)^2 + \left(\frac{\mathrm{Re}\beta}{\mu_{2*}}\right)^2 = 1, \tag{55}$$

where $\mathcal{C}_0 = 1 + \frac{1}{2}\mu_{2*}$. There is an analogy to a linear force field with central point $\mathcal{C}_0 i$. A linear force field acting on β obeys orbital equation (parametrized by t)

$$\frac{d^2\beta}{dt^2} = -(\beta - \mathcal{C}_0 i), \tag{56}$$

whose solution $\beta = \frac{3}{4}\mu_{2*}e^{it} + \frac{1}{4}\mu_{2*}e^{-it} + \mathcal{C}_0 i$ is equivalent to Eq. (55). This analogy implies that $\mathcal{C}_0$ can be seen as a center in the system. This important linear force field analogy encourages us to consider β in the general case as a linear combination of different components, based on the principle of superposition.

Another identity under the condition of $\mu_4 = 0$ that has been found is that surface normal angle ϕ can be written analytically as a function of $\Xi_\parallel$ only by (see Appendix F for derivation)

$$\begin{aligned}\phi^+ &= \frac{\pi}{2} + 2\arcsin\frac{\Xi_\parallel}{\mu_2} - \frac{2(2+\mu_{2*})}{\sqrt{1+\mu_{2*}}} \\ &\quad\times \arctan\left[\frac{1}{\sqrt{1+\mu_{2*}}}\tan\left(\frac{1}{2}\arcsin\frac{\Xi_\parallel}{\mu_2}\right)\right] \\ \text{or } \phi^- &= \frac{\pi}{2} - 2\arcsin\frac{\Xi_\parallel}{\mu_2} - \frac{2(2+\mu_{2*})}{\sqrt{1+\mu_{2*}}} \\ &\quad\times \arctan\left[\frac{1}{\sqrt{1+\mu_{2*}}}\cot\left(\frac{1}{2}\arcsin\frac{\Xi_\parallel}{\mu_2}\right)\right],\end{aligned} \tag{57}$$

where ϕ^+ applies when $\gamma > \gamma_0$ and ϕ^- applies when $\gamma < \gamma_0$. Equation (57) clearly demonstrates that as the normal angle oscillates back and forth around $\pi/2$, the bending stress oscillates around zero. The normal stress is not the source of oscillation.

2. *Higher-order anchoring models*

Similar analysis applies when $\mu_4 \neq 0$ (two loops in the β curve) in quartic model too. In Fig. 13, μ_2 and μ_4 induce two separate β loops such that the net effect of β_2 and β_4 is a Limaçon curve. The physical demonstration of the superposition principle is the two-wavelength surface profile. The average effect, represented by their mean value $\hat{\mu}_* = \frac{1}{2}(\mu_{2*} + \mu_{4*})$, always induces a loop with $W_p = 1$ such that

$$\frac{1}{2\pi i}\oint_\Xi \frac{1}{\beta - \hat{\mu}_*}\, d\beta = 1. \tag{58}$$

Generally, if the surface energy satisfies Eq. (1), then β is a summation of n sub-β such that $\beta = \sum_{j=1}^{n}\beta_{2j}$ where each

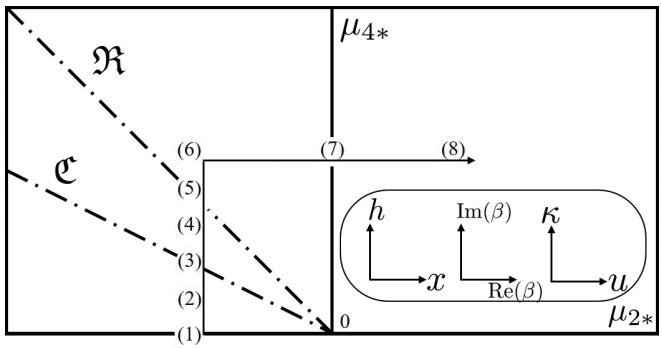

FIG. 10. The first and second quadrant of Λ_4. $\mathfrak{R}$ is the resonance line while $\mathfrak{C}$ is the critical line. (1) to (8) are eight points chosen for further discussion in Figs. 11 and 12 to relate geometry [$h(x)$], mechanics (imaginary part of β as a function of its real $\mathbb{R}$ part), and mechanogeometry [curvature κ as a function of stress ratio $u = \mathrm{Re}(\beta)/\mathrm{Im}(\beta)$].

β_{2j} is a closed path described by

$$(\mathrm{Re}\beta_{2j})^2 = (2j\mu_{2j*})^2\left(\frac{\mathrm{Im}\beta_{2j}}{\mu_{2j*}}\right)^{2-\frac{1}{j}} \times \left[1 - \left(\frac{\mathrm{Im}\beta_{2j}}{\mu_{2j*}}\right)^{\frac{1}{j}}\right], \tag{59}$$

where $\mathrm{Im}\beta_{2j}$ takes the value between 0 and μ_{2j*}. Another important parameter to measure is the portion of each component in β, since it is a basic geometric property and our following discussion is based on admitting β as the core concept. We define $u = \mathrm{Re}(\beta)/\mathrm{Im}(\beta)$. It can be verified that u links capillary vector and surface energy by $\Xi = \gamma\sqrt{1+u^2}$. We choose u to represent mechanics. First, it is a real scalar instead of a complex number β or vector $\boldsymbol{\Xi}$. The main consideration is that we are expected to discuss the topology of the figure, indicating the relationship between mechanics and geometry. Hence, the absolute value of h is less important than its curvature. Similarly, u, which erased the magnitude effect brought by isotropic tension γ_0, is a better parameter to represent mechanics. Notice that there is a natural invariant point in κ-u plot where $\kappa = 2q\mu_{2*}$ and $u = 0$.

We use eight representative points whose locations are given by Fig. 10 to evaluate mechanogeometry relations. We compare h-x pattern (left lower inset), the winding pattern of β in $\mathbb{C}^1$ (middle inset shown as imaginary "i" versus real $\mathbb{R}$ components of β) and κ-u (right inset) in $\mathbb{R}^2$. They represent geometry, mechanics, and mechanogeometry relations, respectively. Numerical results are shown in Fig. 11. The numbers 1–8 correspond to anchoring conditions shown in Fig. 10.

To avoid ambiguities, the following content are discussed within one period only, unless otherwise specified. Firstly, both β and κ-u are closed curves, corresponding to the fact that surface relief pattern is periodic. Another conclusion we draw is that the number of wavelengths in the h-x profile is exactly the winding number W_p of β and κ-u loops. A generalized proposition holds: the number of peaks (or valleys) equals $2 \times W_p$. We may find a contradiction that condition (5) (lying along the resonance line $\mathfrak{R}$) does not match this proposition from observing Fig. 11 at first glance,

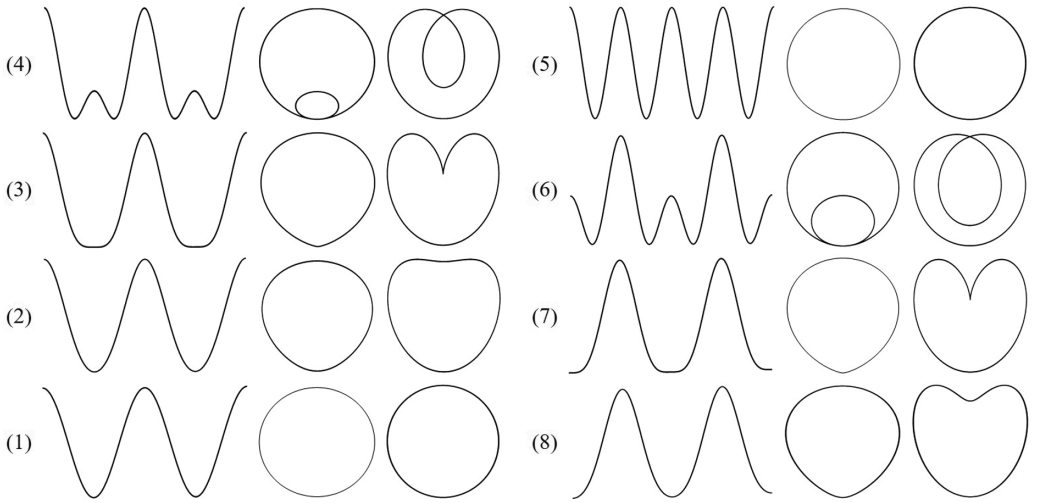

FIG. 11. The comparison of h-x (geometry), β (mechanics), and κ-u (mechanogeometry relationship), for eight (1–8) conditions identified in Fig. 10. In (1–4) the left column is h, the middle is β, and on the right we find κ-u; the same applies to (5–8). In (4) we see that double wrinkling corresponds to inner loops (crossings) in stress and curvatures-stress loops.

since the number of winding for β and κ-u is 1, instead of two corresponding to four peaks in h-x profile. Nevertheless, even if this contradiction seems true, then we just need to modify the proposition to: W_p of $\beta : [0, 1] \to \mathbb{C}$ is half of the peaks in the surface relief. If we move along s on the h-x profile, then β actually rotates twice under condition Eq. (5) by Eq. (52). The two crossings overlap since they are identical. These two identical crossings is the reason why four peaks are identical along $\mathfrak{R}$ in Λ_4.

Points (3) and (7) demonstrate another special condition. What we observed from β and κ-u paths is that those paths have an apparent sharp point (actually it is smooth). It reminds us that the two plateau area (actually not flat) shown in h-x profile too. It can be verified that this sharp point in β or κ-u paths corresponds to the two plateau areas in h-x profile. If we observe β from Eqs. (2) to (4), then Eq. (3) is exactly the point when the emergence of a crossing starts to appear from a smooth path. If we observe h-x in the same way, then we find that Eq. (3) is exactly the point when h-x starts to generate another small wrinkling structure.

If we are moving along $\mathfrak{R}$, then h-x, β, and κ-u should only change magnitudes rather than topology. This is demonstrated by Fig. 12. An interesting phenomenon is that there is an invariant point for β while for κ-u the path changes proportional

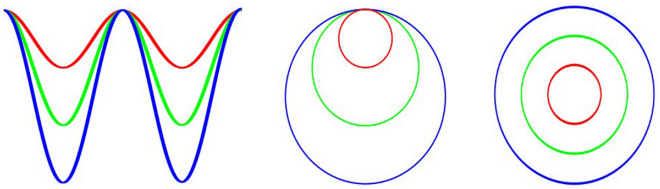

FIG. 12. Magnitudes of surface profile $h(x)$ (left), Lamé stress curve β (middle) and curvature-stress ratio loop κ-u (right) and how they change along the resonance line $\mathfrak{R}$ while maintaining their topology ($3 \times \mu_{\text{Red}} = 2 \times \mu_{\text{Green}} = \mu_{\text{Blue}}$). Moving radially in the anchoring diagram (Fig. 10) only changes amplitudes. This figure only shows half the period $P_0/2$.

with respect to its central point. The invariant point in β is $\text{Re}\beta = 0$ and $\text{Im}\beta = 1$ as discussed in Table II. But for u, the invariant has been erased.

We can extend our discussion to arrive at a general result. Recall that $\tilde{h} = \sum_{j=1}^{n} \tilde{h}_{2j}$ where $\tilde{h}_{2j} = \frac{1}{q}\mu_{2j*} \sin^{2j} qx$, and $\beta = \sum_{j=1}^{n} \beta_{2j}$. A surface relief can be seen as a superposition of subrelief $\tilde{h}_{2j}$, where each one is dependent on μ_{2j*}. Similarly, β can be seen as the summation of sub-β β_{2j}. We bring another structure to the h profile and β topology each time we add another nonvanishing anchoring coefficient μ_{2j*}. Each pattern of surface relief has an inverse pattern (just switch the sign of $\boldsymbol{\mu}$ or P_0, as shown in Sec. III A) and they add pointwise to flat surface (where $\boldsymbol{\mu} = \mathbf{0}$). For β, we assign a direction to the path such we define the positive direction to be the trend of the movement of $(\Xi_{\parallel}, \Xi_{\perp})$ when x is increasing in $h(x)$. We also assign the starting point as the point where $x = 0$ ($\beta = i$ at this point). If we switch the sign of $\boldsymbol{\mu}$ or P_0, then we will not reverse the direction of β. However, we reverse the velocity to this point. The reversed β and the original one can add to zero too (where $\boldsymbol{\mu} = \mathbf{0}$, see the bottom left figure of Fig. 14).

We use a quartic model in Fig. 13 to demonstrate this fact. The surface pattern and β in Λ_4 can be seen as a direct superposition of that in Λ_2, and that brought by μ_4. Previously we have shown that a two-wavelength pattern can only be found in certain area in the second and fourth quadrant (see Fig. 3). Now we can explain this phenomenon easily with Fig. 13. In those two quadrants, μ_2 and μ_4 have the opposite sign. They assign opposite starting velocity to the β_2 and β_4 path with same starting point ($\beta = i$ at this point). Hence, the net result is when two starting points glued together and satisfy the algebra such that the imaginary part and real part are added separately. Figure 14 shows a summary of stress loops superposition and the resulting Limaçons, corresponding to five conditions of Fig. 10. The underlying phenomena are:

Condition (2), $|\mu_{4*}| < |\frac{1}{2}\mu_{2*}|$: The magnitude of μ_4 is too small to generate another loop. W_p still remains at 1 due to μ_{2*};

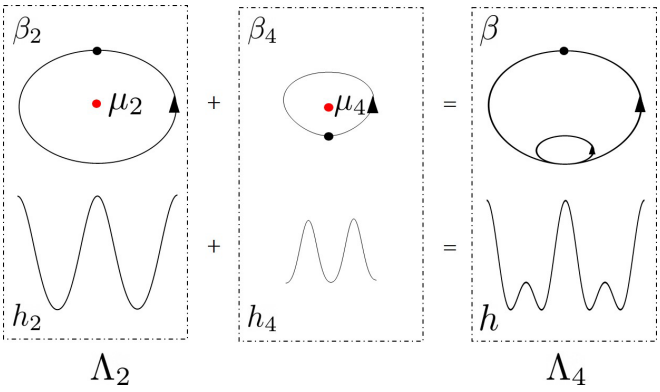

FIG. 13. A sketch explaining how $h(x)$ and β can be seen as a direct superposition of their components in quartic model. Here, red point represents the center introduced by each anchoring coefficient. Black point represents the starting point, which is also the point where β_2 and β_4 are glued together.

Condition (3), $|\mu_{4*}| = |\frac{1}{2}\mu_{2*}|$: This condition corresponding to critical line, β_4 generated by μ_{4*} is larger, and is the critical point across which β exhibits a jump from $W_p = 1$ to $W_p = 2$;

Condition (4), $|\frac{1}{2}\mu_{2*}| < |\mu_{4*}| < |\mu_{2*}|$: The effect of μ_{4*} becomes greater enough to generate another loop, thus $W_p = 2$. And this small loop corresponds to μ_{4*};

Condition (5), $|\mu_{4*}| = |\mu_{2*}|$: The small loop created by μ_{4*} increases and now is able to overlap with the big loop generated by μ_{2*}, so $W_p = 2$;

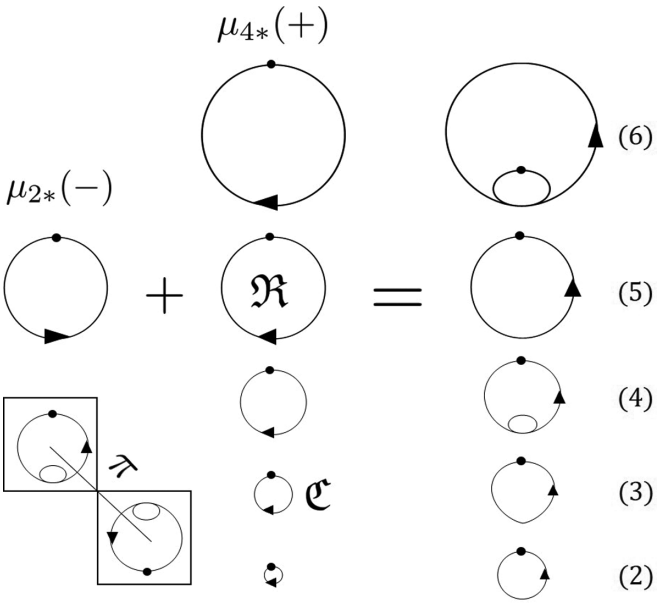

FIG. 14. Stress loop superposition and resulting Limaçon curves. A summary of how five conditions of β_2 and β_4 in the second quadrant of Λ_4. The number on the right represents its corresponding position in Fig. 10. And the black point on the loop represents the starting point, which is the first invariant point in Table II, and the point where β_2 and β_4 are glued together. The subfigure on the bottom left represents how the π rotation symmetric point (fourth quadrant) behave.

Condition (6), $|\mu_{4*}| > |\mu_{2*}|$: The effect brought by μ_4 is so large such that the role between μ_{2*} and μ_{4*} exchanges. If we fix the invariant point in μ_{2*}, then to increase the μ_{4*} loop, the final result must be the case shown as condition (6) in Fig. 14, where the starting point now moved to the smaller loop. Hence, if we observe conditions (4) and (6), then the only difference is where the starting point is, so the surface profiles $h(x)$ for conditions (4) and (5) are just a phase shift apart.

In the first and third quadrant, μ_2 and μ_4 assign same starting points to β paths, therefore the net effect is just a larger Lamé curve instead of creating a two-wavelength surface pattern. The third and fourth quadrant are symmetric to the first and second quadrant, thus can be analyzed by similar way. In the bottom left subfigure of Fig. 14, we can see that the symmetric point on the fourth quadrant with respect to that on the second quadrant corresponds to a β curve which is also a π rotation with respect to that of the second quadrant, while maintaining the same winding number. What is more, winding number does not change its sign when we are moving on Λ_4, and this will be explained in Appendix E.

A more mathematical statement, that confirms the numerical results of Fig. 11, is that from the Abelian group of surface patterns $h(x)$ (geometry) with operation $+$ to the Abelian group of complex capillary vector parameter β (mechanics) with directed loop addition, there is a map $Y(h \to \beta)$ which preserves group structure. This map $Y(h \to \beta)$ is called a homomorphism, and is the fundamental mechanogeometry relation of this paper.

In partial summary, we established a link between the topology of the Lamé stress curves and the geometric surface relief and used superposition principles to explain the generation of double wrinkling by taking into account the circulation direction in the stress loops. The mathematical homeomorphism result finds direct applications when assigning stress fields to wrinkled surfaces.

3. Matrix representation of mechanogeometry relation

Rotation matrix $\mathbf{R}(a)$ transforms a vector counterclockwise by angle of a and can be expressed by

$$\mathbf{R}(a) = \begin{bmatrix} \cos a & \sin a \\ -\sin a & \cos a \end{bmatrix}. \tag{60}$$

The special rotation matrix $\mathbf{R} = \mathbf{tk} - \mathbf{kt}$ we introduced in Eq. (18) is just $\mathbf{R}(\frac{\pi}{2})$. Then $\mathbf{k} = \mathbf{t} \cdot \mathbf{R}$ and $\mathbf{T}_v = \boldsymbol{\Xi} \cdot \mathbf{R}$. The mechanical frame $(\boldsymbol{\Xi}, \mathbf{T}_v)$ and geometric frame $(\mathbf{t}, \mathbf{k})$ can be integrated as

$$[\boldsymbol{\Xi} \quad \mathbf{T}_v] = -[\mathbf{t} \quad \mathbf{k}] \cdot \underbrace{\begin{bmatrix} \partial_\theta \gamma & \gamma \\ -\gamma & \partial_\theta \gamma \end{bmatrix}}_{\mathbf{Y}}, \tag{61}$$

where the Jacobian transformation matrix $\mathbf{Y}$ contains the information of both mechanics (γ) and geometry (∂_θ). $[\mathbf{t}\ \mathbf{k}]$ represents pure geometry, and $[\boldsymbol{\Xi}\ \mathbf{T}_v]$ represents pure mechanics. Hence, $\mathbf{Y}$ is a matrix representation of this mechanogeometry relation. An observation from Eqs. (60) and (61) yields the following identity:

$$\mathbf{Y} = \gamma\sqrt{1+u^2}\mathbf{R}(\text{arccot}u) = \boldsymbol{\Xi}\mathbf{R}(\text{arccot}u). \tag{62}$$

This relation can be shown in Fig. 1. The area spun by $\mathbf{T}_v$ and $\boldsymbol{\Xi}$ is just a rotation of the area spun by $\mathbf{k}$ and $\mathbf{t}$ scaled by Ξ with angle arccot$u$. Matrix $\mathbf{R}(a) \in \mathrm{SO}(2)$ and can be represented by

$$\mathrm{Diag}\mathbf{R}(a) = \begin{bmatrix} \cos a - i \sin a & 0 \\ 0 & \cos a + i \sin a \end{bmatrix} = \begin{bmatrix} e^{ia} & 0 \\ 0 & e^{ia} \end{bmatrix}, \tag{63}$$

which reminds us the matrix form $\mathbf{B}$ in Eq. (49) by observing the similarity between Eqs. (49) and (63). Hence, $\mathbf{Y}$ can also be decomposed in the similar way of $\mathbf{B}$,

$$\mathbf{Y} = \partial_\theta \gamma \mathbf{I} + \gamma \mathbf{R}. \tag{64}$$

Comparing the decomposition of $\mathbf{Y}$ with Eq. (48), we found that $\mathbf{Y} + \mathbf{B} = 2\gamma\mathbf{R}$. The eigenvalues of $\mathbf{Y}$ is simply

$$\lambda_\pm = \underbrace{\gamma\sqrt{1+u^2}}_{\text{stretch}} \cdot \underbrace{[\cos(\text{arccot}u) \pm i \sin(\text{arccot}u)]}_{\text{rotation}}, \tag{65}$$

with eigenvectors

$$\mathbf{V}_{\lambda_+} = [i \quad 1]t \quad \text{and} \quad \mathbf{V}_{\lambda_-} = [-i \quad 1]t, \tag{66}$$

where t is any nonvanishing real constant. Ξ is the Pfaffian of $\mathbf{Y}$. $\mathbf{Y}$ transforms geometry to mechanics, so $\mathbf{Y}^{-1}$ reverses this process. To ensure $\mathbf{Y}^{-1}$ exists, we need $\det\mathbf{Y} \neq 0$, which always holds due to $\gamma > 0$ and $u \geqslant 0$.

In partial summary, we show that a simple nonsingular rotation-dilation Jacobian transformation matrix [Eq. (64)] incorporates the geometry and mechanics relations. In practice, fast matrix solvers can be used for any anchoring model order to find stresses from geometry and vice versa. After all the variables defined as before, we can finally summarize our main results to the following diagram:

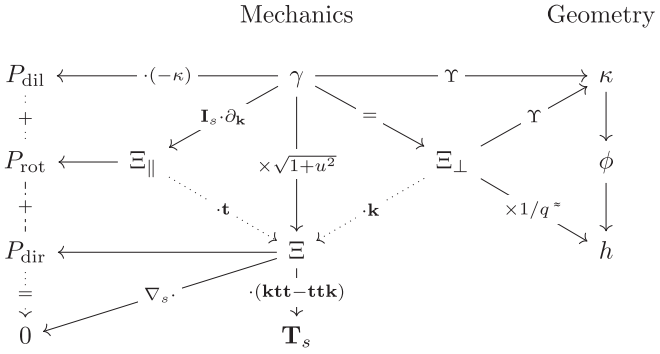

where $\approx$ connecting two parameters represent that they are equivalent within the linear region.

VI. CONCLUSIONS

This paper presents a comprehensive formulation, analysis, and characterization of surface wrinkling in cholesteric liquid crystals, as precursors of the ubiquitous biological plywoods found in nature. The central focus of the paper is to establish all the possible links between wrinkling geometry and mechanical stresses methods that emphasize scaling laws, topological invariants, and parameter-free generic features of geometry and mechanics. Details of the mathematical foundations were shifted to the appendices and whenever possible contact with real applications were made. For wrinkling to occur, the surface tension must be anisotropic, and generic anchoring models of increasing order were considered.

The shape equations for wrinkled cholesteric surfaces were developed using capillary pressure [Eq. (19)], capillary vector [Eq. (29)], and least action [Eq. (31)] models. They all converge to the same equation by emphasize different aspects of wrinkling, such as the fundamental role of director capillary pressure in causing wrinkling. Also the pendulum analogy (Sec. II D) common in capillary models is shown to exist in this anisotropic surfaces. Using linearization (Sec. II E), we find important insights to wrinkling geometry, geometric symmetry and chirality. Importantly we show how a change in the sign of the cholesteric pitch changes the surfaces. Since the motivation of the work is to eventually correlate geometry to optical, tribological, wetting, and cell growth functionalities, we characterized the moments of the surface geometry, in particular the arithmetic mean, kurtosis, and skewness, and obtained anchoring parameters relations that maximize or minimize these functions. In particular, for a quartic anchoring model we found that the applications important kurtosis-skewness curve is a universal parameter-free bifolium, whose extrema can be found by tuning anchoring (Fig. 6).

The wrinkling mechanics was characterized by polar capillary pressure plots that unequivocally show that dilation pressure is essentially balanced the driving director pressure. Also we establish a connection with classical Lamé stress curves for materials with 2D stresses. Introducing a complex capillary number whose real component is the negative of the bending stress and whose imaginary component is the normal (dilation) stress we find that our anchoring-driven wrinkling generates Limaçon stress loops that generalize the simpler Lamé ellipses. The topological charge of this stress loop in terms of a winding number is found in terms of any anchoring model (Fig. 8). Equally important the maximum winding numbers reflects the bending stress landscape, since the higher it is the more sign changes we find in this important stress component. Finally, synthesis all results in Fig. 11, establishing the connections between surface relief, Lamé stress loops, and curvature-stress ratio Limaçons. The mechanogeometry connections is shown to be a rotation-dilation Jacobian matrix whose spectral decomposition involve stress information.

Finally, we synthesize the geometry, mechanics, mechanogeometry relations into a flow-chart that reveals their interconnections. At the center we find the surface tension γ and capillary vector $\boldsymbol{\Xi}$ and from these we valuate pressures, stresses, and curvature. Reflecting the various shape equation formulations we can find curvature κ in two different ways. Finally, the surface relief h is found from curvature or in the linear approximation from anisotropic tension.

Taken together these results provide a comprehensive picture of surface wrinkling by anchoring mechanisms that can in the future be extended to two-wave-vector wrinkling, nematic and smectic liquid crystals, bulk elasticity corrections, transient emerging pattern formation, and active liquid crystals and chiral mass transfer [49–53].

ACKNOWLEDGMENTS

This work is supported by the Natural Science and Engineering Research Council of Canada Discovery Grants (NSERC DG, Grant No. 223086). A.D.R. is grateful for financial support through the James McGill Professorship program at McGill University. We acknowledge Compute Canada for computational resources and technical support.

APPENDIX A: ENERGY REDUCTION BY WRINKLING

In this Appendix, we will use an efficient geometric method to prove that wrinkling reduces surface energy. Let us simplify our discussion by assuming that $\mu_{4*} = 0$. Surface energy density for a specific wrinkling pattern is

$$\frac{E_w}{\gamma_0} = \left(\int_0^{P_0} \frac{1}{\sin\phi}\,dx\right)^{-1} \int_0^{P_0} [1 + \mu_{2*}(\mathbf{n}\cdot\mathbf{k})^2]\frac{1}{\sin\phi}\,dx. \tag{A1}$$

Flat surface under the same anchoring condition is

$$\frac{E_f}{\gamma_0} = \frac{1}{P_0}\int_0^{P_0} [1 + \mu_{2*}(\mathbf{n}\cdot\hat{\boldsymbol{\delta}}_y)^2]\,dx, \tag{A2}$$

where $\hat{\boldsymbol{\delta}}_y$ is the unit vector along y axis (perpendicular to x axis). Rearranging Eqs. (A1) and (A2). To prove $E_w < E_f$, we just need to show

$$\int_0^{P_0} \mu_{2*}(\mathbf{n}\cdot\hat{\boldsymbol{\delta}}_y)^2\,dx > \int_0^{P_0} \mu_{2*}(\mathbf{n}\cdot\mathbf{k})^2\frac{1}{\sin\phi}\,dx, \tag{A3}$$

since the following inequality already holds:

$$\left(\int_0^{P_0} \frac{1}{\sin\phi}\,dx\right)^{-1} < \frac{1}{P_0}. \tag{A4}$$

Our question simplifies to prove Eq. (A3) holds $\forall\mu_{2*} \in \mathbb{R}^+$. First, if $\mu_{2*} < 0$, then we only need to prove

$$\int_0^{P_0} (\mathbf{n}\cdot\hat{\boldsymbol{\delta}}_y)^2\,dx < \int_0^{P_0} (\mathbf{n}\cdot\mathbf{k})^2\,dx, \tag{A5}$$

since

$$\int_0^{P_0} (\mathbf{n}\cdot\mathbf{k})^2\,dx < \int_0^{P_0} (\mathbf{n}\cdot\mathbf{k})^2\frac{1}{\sin\phi}\,dx. \tag{A6}$$

Notice that $\mathbf{n}$, $\mathbf{k}$, and $\hat{\boldsymbol{\delta}}_y$ are unit vectors. The volume form $\mathrm{vol}_2 = \sqrt{\det(\mathbf{G})}dx \wedge dy$, where $\mathbf{G}$ is the metric tensor. Since $\mathbf{a}\times\mathbf{b} = *(\mathbf{a}\wedge\mathbf{b})$, where $*$ is the Hodge star operator, so we can use cross product to represent an area in $\mathbb{R}^3$. Equation (A5) can be transformed to

$$P_0 - \int_0^{P_0} (\mathbf{n}\times\hat{\boldsymbol{\delta}}_y)^2\,dx < P_0 - \int_0^{P_0} (\mathbf{n}\times\mathbf{k})^2\,dx. \tag{A7}$$

We just need to show that $(\mathbf{n}\times\hat{\boldsymbol{\delta}}_y)^2 > (\mathbf{n}\times\mathbf{k})^2$ is true for every position on surface.

From Fig. 15 we can see that $\|\mathbf{n}\times\hat{\boldsymbol{\delta}}_y\| > \|\mathbf{n}\times\mathbf{k}\|$ since $h_2 > h_1$, where h_2 is the height of $\|\mathbf{n}\times\hat{\boldsymbol{\delta}}_y\|$ and h_1 is the height of $\|\mathbf{n}\times\hat{\boldsymbol{\delta}}_y\|$.

For $\mu_{2*} > 0$, to prove Eq. (A3), we only need to show

$$\int_0^{P_0} (\mathbf{n}\cdot\hat{\boldsymbol{\delta}}_y)^2\,dx > \int_0^{P_0} \left(\mathbf{n}\cdot\frac{\mathbf{k}}{\sin\phi}\right)^2 dx, \tag{A8}$$

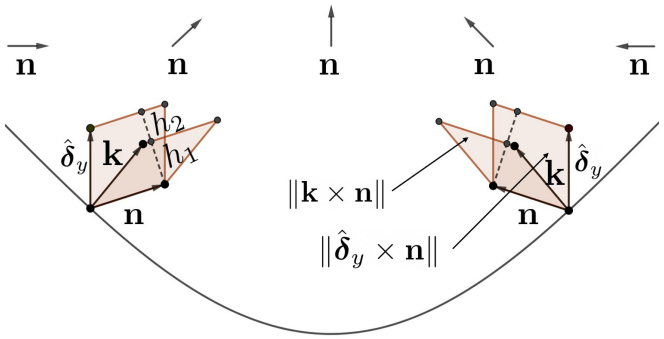

FIG. 15. Surface profile when $\mu_2 < 0$.

since

$$\int_0^{P_0} \left(\mathbf{n}\cdot\frac{\mathbf{k}}{\sin\phi}\right)^2 dx > \int_0^{P_0} (\mathbf{n}\cdot\mathbf{k})^2\frac{1}{\sin\phi}\,dx. \tag{A9}$$

Similarly, Eq. (A8) can be transformed to

$$P_0 - \int_0^{P_0} (\mathbf{n}\times\hat{\boldsymbol{\delta}}_y)^2\,dx > P_0\int_0^{P_0}\frac{1}{\sin^2\phi}\,dx - \int_0^{P_0}\left(\mathbf{n}\times\frac{\mathbf{k}}{\sin\phi}\right)^2 dx. \tag{A10}$$

Rearrange the inequality above such that

$$0 > P_0\left(1 - \int_0^{P_0}\frac{1}{\sin^2\phi}\,dx\right) > \int_0^{P_0}(\mathbf{n}\times\hat{\boldsymbol{\delta}}_y)^2\,dx - \int_0^{P_0}\left(\mathbf{n}\times\frac{\mathbf{k}}{\sin\phi}\right)^2 dx. \tag{A11}$$

Thus, we only need to show that

$$\int_0^{P_0}\left(\mathbf{n}\times\frac{-\mathbf{k}}{\sin\phi}\right)^2 dx > \int_0^{P_0}(\mathbf{n}\times-\hat{\boldsymbol{\delta}}_y)^2\,dx. \tag{A12}$$

The negative sign here is to reverse the direction of each vector. In Fig. 16, we define point D_1 to be the reflection of point B with respect to point O such that $\overline{OB}\cdot\overline{OD_1} = 1$, then we define point D_2 such that $\overline{OD_2} = \overline{OD_1}$. Hence, we find that $\overrightarrow{OD_2}$ is exactly $-\mathbf{k}/\sin\phi$ and $\overrightarrow{OC}$ is $-\hat{\boldsymbol{\delta}}_y$.

Draw a similar figure as we did in Fig. 15, the new figure under this condition is shown as Fig. 17. Hence, $\|-\mathbf{k}\times\mathbf{n}/\sin\phi\| > \|-\hat{\boldsymbol{\delta}}_y\times\mathbf{n}\|$ due to $h_2 > h_1$. Also notice that in Figs. 15 and 17, sometimes $\mathbf{n}$ can be stuck in the middle of $\mathbf{k}$ and $\hat{\boldsymbol{\delta}}_y$. However, in weak wrinkling $\mathbf{k} \approx \hat{\boldsymbol{\delta}}_y$. There is almost no contribution to the integral in Eq. (A3) under this condition. In summary, we have proved that for both cases when $\mu_2 > 0$ and $\mu_2 < 0$, $E_w < E_f$. And when $\mu_2 = 0$, $E_w = E_f$, which is the trivial case where the surface is completely flat. The condition under which $\mu_4 \neq 0$ can be analyzed by the same way, then we can linearly add them up to conclude that wrinkling reduces energy.

In partial summary, the static formulation used in this paper always generates solutions that decrease total energy.

Here we explain why Eq. (16) vanishes. For cholesteric liquid crystal where $q \neq 0$ the function $f_g(\mathbf{n}, \nabla\mathbf{n})$ is greater than 0 for any $\mathbf{n} \in \mathbb{S}^2$, and $\nabla\mathbf{n} \in \mathbb{GL}(3)$ if and only if

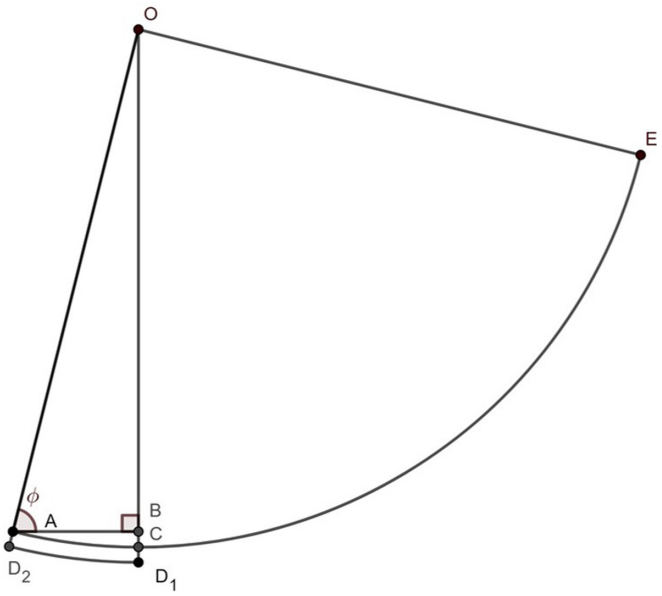

FIG. 16. Surface vector sketch when $\mu_2 > 0$.

$K_2 + K_4 = 0$ [54]. Hence, $\gamma_g = \frac{1}{2}(K_2 + K_4)\mathbf{k}\cdot\mathbf{g} = 0$, we only need to evaluate the first term of $\mathbf{h}$, where

$$\mathbf{hk} : (\nabla\mathbf{n})^\intercal = (\mathbf{I} - \mathbf{nn}) \cdot \left(\sum_{j=1}^{\infty} 2j\mu_{2j}(\mathbf{n}\cdot\mathbf{k})^{2j-1}\right)\mathbf{k} : (\nabla\mathbf{n})^\intercal$$

$$= \left(\sum_{j=1}^{\infty} 2j\mu_{2j}(\mathbf{n}\cdot\mathbf{k})^{2j}\right)\mathbf{kk} : (\nabla\mathbf{n})^\intercal, \tag{A13}$$

we just need to show $\mathbf{kk} : (\nabla\mathbf{n})^\intercal \to 0$. Then Eq. (16) naturally vanishes. First, according to the assumed director field, $\mathbf{n}_y$ is only a function related to x, so $\hat{\boldsymbol{\delta}}_y\hat{\boldsymbol{\delta}}_y : (\nabla\mathbf{n})^\intercal = 0$:

$$\mathbf{kk} = \mathbf{kk}|_{\hat{\boldsymbol{\delta}}_y} + \left.\frac{\partial\mathbf{kk}}{\partial\mathbf{k}}\right|_{\hat{\boldsymbol{\delta}}_y} \cdot (\mathbf{k} - \hat{\boldsymbol{\delta}}_y) + \mathcal{O}(2)$$

$$= \hat{\boldsymbol{\delta}}_y\hat{\boldsymbol{\delta}}_y + (\mathbf{I}\hat{\boldsymbol{\delta}}_y + \hat{\boldsymbol{\delta}}_y\mathbf{I}) \cdot (\mathbf{k} - \hat{\boldsymbol{\delta}}_y) + \mathcal{O}(2).$$

Therefore,

$$\mathbf{kk} : (\nabla\mathbf{n})^\intercal = (\mathbf{I}\hat{\boldsymbol{\delta}}_y + \hat{\boldsymbol{\delta}}_y\mathbf{I}) \cdot (\mathbf{k} - \hat{\boldsymbol{\delta}}_y) : (\nabla\mathbf{n})^\intercal \sim \cos\phi. \tag{A14}$$

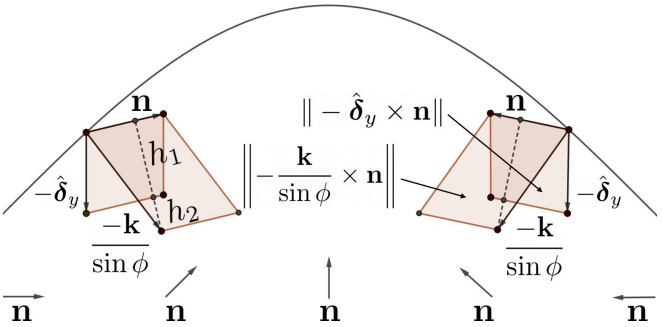

FIG. 17. Surface profile when $\mu_2 > 0$.

Now we can evaluate $\cos\phi$

$$-\frac{\cos\phi}{\sin\phi} = \frac{dh}{dx} = \sum_{j=1}^{n} 2j\mu_{2j*}\sin^{2j-1} qx\cos qx$$

$$= \sum_{j=1}^{n} j\mu_{2j*}\sin^{2j-2} qx\sin 2qx \tag{A15}$$

and find the following bounds:

$$-\sum_{j=1}^{n} j\mu_{2j*} \ll -\frac{\cos\phi}{\sin\phi} \ll \sum_{j=1}^{n} j\mu_{2j*}, \tag{A16}$$

since μ_{2j*} are very close to 0, so $\cos\phi \to 0$.

APPENDIX B: STRESS TENSOR

In this Appendix, we will derive the formula of stress tensor $\mathbf{T}_s$ that appears in Eq. (18).

A small displacement $\mathbf{u}$ gives a small change of the energy δF,

$$\delta F = \int \mathbf{T}_B : (\nabla_s\mathbf{u})^\intercal\, d\Theta, \tag{B1}$$

where Θ represents area. The variation of energy can also be expressed in terms of the energy change

$$\delta F = \int \mathbf{I}_s \cdot \frac{d\gamma}{d\mathbf{k}}\delta\mathbf{k}\, d\Theta$$

$$= \int \mathbf{I}_s \cdot \frac{d\gamma}{d\mathbf{k}}[-\mathbf{k}\cdot(\nabla_s\mathbf{u})^\intercal]\, d\Theta. \tag{B2}$$

Compare these two expressions and we can obtain

$$\mathbf{T}_B = -\mathbf{I}_s \cdot \frac{d\gamma}{d\mathbf{k}} \otimes \mathbf{k}, \tag{B3}$$

while the tension is

$$\mathbf{T}_N = \gamma\mathbf{I}_s. \tag{B4}$$

Hence, stress tensor is written as

$$\mathbf{T}_s = \gamma\mathbf{I}_s - \mathbf{I}_s \cdot \frac{d\gamma}{d\mathbf{k}} \otimes \mathbf{k}. \tag{B5}$$

APPENDIX C: GEOMETRIC CHARACTERIZATION

This Appendix is to derive Eqs. (41) and (42), along with proofs to some conclusions in Sec. III.

To derive Eq. (41), let us denote

$$I_n = \int \sin^n x\, dx, \tag{C1}$$

integrating I_n by part gives us

$$I_n = \int \sin^{n-1} x\, d(-\cos x)$$

$$= -\cos x\sin^{n-1} x + \int \cos^2 x(n-1)\sin^{n-2} x\, dx$$

$$= -\cos x\sin^{n-1} x + (n-1)\int (1-\sin^2 x)\sin^{n-2} x\, dx$$

$$= -\cos x\sin^{n-1} x + (n-1)\int \sin^{n-2} x\, dx$$

$$-(n-1)\underbrace{\int \sin^n x\, dx}_{I_n}. \tag{C2}$$

Combine term I_n so we can obtain

$$I_n = \int \sin^n x\,dx = -\frac{1}{n}\cos x \sin^{n-1} x + \left(1-\frac{1}{n}\right)\int \sin^{n-2} x\,dx. \tag{C3}$$

Compute the proper integral and replace x with qx. Also notice that $\cos(qP_0) = \cos 0$ and $\sin(qP_0) = \sin 0$. Assume n is an even number:

$$\begin{aligned}\int_0^{P_0} \sin^n(qx)\,dx &= -\frac{1}{qn}\cos(qx)\sin^{n-1}(qx)\Big|_0^{P_0} + \left(1-\frac{1}{n}\right)\int_0^{P_0}\sin^{n-2}(qx)\,dx \\ &= \left(1-\frac{1}{n}\right)\int_0^{P_0}\sin^{n-2}(qx)\,dx \\ &= P_0\prod_{i=1}^{n/2}\left(1-\frac{1}{2i}\right).\end{aligned} \tag{C4}$$

Notice that the last term is equivalent to

$$\prod_{i=1}^{n/2}\left(1-\frac{1}{2i}\right) = \frac{\left(2\times\frac{n}{2}-1\right)!!}{2^{\frac{n}{2}}\left(\frac{n}{2}\right)!} = \frac{1}{\sqrt{\pi}}\frac{\Gamma\left(\frac{n}{2}+\frac{1}{2}\right)}{\Gamma\left(\frac{n}{2}+1\right)}. \tag{C5}$$

Therefore, we can easily find that

$$\int_0^{P_0}\sin^n(qx)\,dx = P_0\mathfrak{b}_{\frac{n}{2}}. \tag{C6}$$

Now we are able to compute $\tilde{M}[n]$

$$\begin{aligned}\tilde{M}[n] &= \frac{1}{P_0}\sum_{i=0}^{n}\binom{n}{i}(-\tilde{m})^{n-i}\int_0^{P_0}\tilde{h}(x)^{(i)}\,dx \\ &= \frac{1}{P_0}\sum_{i=0}^{n}\binom{n}{i}(-\tilde{m})^{n-i} \\ &\quad\times\int_0^{P_0}(\mu_{2*}\sin^2 qx + \mu_{4*}\sin^4 qx)^i\,dx \\ &= \frac{1}{P_0}\sum_{i=0}^{n}\binom{n}{i}(-\tilde{m})^{n-i} \\ &\quad\times\sum_{j=0}^{i}\binom{i}{j}\mu_{2*}^j\mu_{4*}^{i-j}\int_0^{P_0}\sin^{2(2i-j)}\,dx \\ &= \sum_{i=0}^{n}\binom{n}{i}(-\tilde{m})^{n-i} \\ &\quad\times\sum_{j=0}^{i}\binom{i}{j}\mu_{2*}^j\mu_{4*}^{i-j}\prod_{t=1}^{2i-j}\left(1-\frac{1}{2t}\right).\end{aligned} \tag{C7}$$

Now we can find the extreme values of m and σ in the quartic model if forcing a restriction $\mu_{2*}^2+\mu_{4*}^2 = C^2$. $\tilde{m} = (\mathfrak{b}_1\mu_{2*}+\mathfrak{b}_2\mu_{4*})/q$, we can construct L_m and L_σ by

$$\begin{aligned}L_m &= \frac{1}{q}(\mathfrak{b}_1\mu_{2*}+\mathfrak{b}_2\mu_{4*}) - \lambda_m\left(\mu_{2*}^2+\mu_{4*}^2-C^2\right), \\ L_\sigma &= \frac{1}{q^2}\left[\left(\mathfrak{b}_2-\mathfrak{b}_1^2\right)\mu_{2*}^2 + 2(\mathfrak{b}_3-\mathfrak{b}_1\mathfrak{b}_2)\mu_{2*}\mu_{4*} + \left(\mathfrak{b}_4-\mathfrak{b}_2^2\right)\mu_{4*}^2\right] - \lambda_\sigma\left(\mu_{2*}^2+\mu_{4*}^2-C^2\right).\end{aligned} \tag{C8}$$

The following equation must satisfy at those extrema

$$\frac{\partial L_m}{\partial\mu_{2*}} = \frac{\partial L_m}{\partial\mu_{4*}} = \frac{\partial L_m}{\partial\lambda_m} = \frac{\partial L_\sigma}{\partial\mu_{2*}} = \frac{\partial L_\sigma}{\partial\mu_{4*}} = \frac{\partial L_\sigma}{\partial\lambda_\sigma} = 0. \tag{C9}$$

Hence, we can solve that when m reaches extremum

$$\mu_{4*} = \frac{\mathfrak{b}_2}{\mathfrak{b}_1}\mu_{2*} = \frac{3}{4}\mu_{2*}. \tag{C10}$$

And when σ reaches extremum

$$\mu_{4*} = \pm\sqrt{\frac{\left(\mathfrak{b}_2-\mathfrak{b}_1^2\right)}{\left(\mathfrak{b}_4-\mathfrak{b}_2^2\right)}}\mu_{2*} = \pm\sqrt{\frac{16}{17}}\mu_{2*}. \tag{C11}$$

We can show that in Λ_{2n} model, the line along which m reaching extremum is perpendicular to the hyperplane where m vanishes. The Lagrangian $L_m = \sum_{i=1}^n \mathfrak{b}_i\boldsymbol{\mu}_{2i*}/q - \lambda_m\sum_{i=1}^n(\mu_{2i*}^2)$. The partial derivative of L_m with respect to μ_{2i*} gives us $\mathfrak{b}_i - 2\lambda_m\mu_{2*} = 0$. Any line inside the hyperplane $\sum_{i=1}^n \mathfrak{b}_i\boldsymbol{\mu}_{2i*}/q = 0$ can be given too. We take the inner product between them,

$$\frac{a}{2\lambda_m}[\mathfrak{b}_1\ \ \mathfrak{b}_2\ \ldots\ \mathfrak{b}_n]\cdot b\left[\mu_{2*}\quad \mu_{4*}\quad \ldots\quad \frac{\sum_{i=1}^{n-1}\mathfrak{b}_i\boldsymbol{\mu}_{2i*}}{\mathfrak{b}_n}\right] = 0, \tag{C12}$$

where a and b are just two nonzero parameters. Hence, this hyperplane is perpendicular to the line where m vanishes.

Now we can discuss the upper limit of σ. A vector $\boldsymbol{\mu}\in\Lambda_{2n}$ whose ith component is μ_{2i*}, and a vector with same dimension $\mathbf{S_I}$ whose ith component is $\sin^{2i} qx$ together form the components of σ^2:

$$\sigma^2 = \frac{1}{q^2P_0}\int_0^{P_0}(\boldsymbol{\mu}\cdot\mathbf{S_I})^2dx - \left[\frac{1}{qP_0}\int_0^{P_0}(\boldsymbol{\mu}\cdot\mathbf{S_I})dx\right]^2. \tag{C13}$$

Notice that the second term can be integrated directly, which becomes $P_0\sum_{i=1}^n \mathfrak{b}_i\mu_{2i*}$, while the first term can be simplified by using Cauchy-Schwarz inequality:

$$\begin{aligned}(q\sigma)^2 &\leqslant \frac{1}{P_0}\int_0^{P_0}|\boldsymbol{\mu}|^2|\mathbf{S_I}|^2dx - \left(\sum_{i=1}^n\mathfrak{b}_i\mu_{2i*}\right)^2 \\ &= \left(\sum_{i=1}^n\mathfrak{b}_{2i}\right)\left(\sum_i^n\mu_{2i*}^2\right) - \left(\sum_{i=1}^n\mathfrak{b}_i\mu_{2i*}\right)^2.\end{aligned} \tag{C14}$$

The two sides are equal if and only if $\boldsymbol{\mu}$ and $\mathbf{S_I}$ are linearly dependent, which is impossible since $\mathbf{S_I}$ is not a constant vector. Hence, we obtained the upper limit of the standard deviation for a given anchoring model.

APPENDIX D: EXTREMA OF MEAN ROUGHNESS (SEC. III B 1)

In this Appendix we analyze extrema in the mean roughness of the surface relief under the assumption that the

anchoring coefficients decrease according to the reasonable assumption $\mu_{2i*} = \alpha \mathfrak{b}_i$ where α is a positive number.

First, we show that series $\{\mathfrak{b}_n\}$ and $\{\mathfrak{b}_n^2\}$ diverge. To prove that, we are encouraged to find the two boundaries by Gautschi's inequality [55] by observing $0 < \mathfrak{b}_n < 1$:

$$\frac{1}{n} > \left[\frac{\Gamma\left(n+\frac{1}{2}\right)}{\Gamma(n+1)}\right]^2 > \frac{1}{n+1}. \tag{D1}$$

Let $f : [1, \infty) \to \mathbb{R}_+$ and $f(n) = \mathfrak{b}_n^2$. Process the integral test such that

$$\begin{aligned}\int_1^\infty f(n)\,dn &= \lim_{t\to\infty}\int_1^t \frac{1}{\pi}\left(\frac{\Gamma\left(n+\frac{1}{2}\right)}{\Gamma(n+1)}\right)^2 dn \\ &> \frac{1}{\pi}\lim_{t\to\infty}\int_1^t \frac{1}{n+1}\,dn \\ &= \frac{1}{\pi}\lim_{t\to\infty}\ln(n+1)|_1^t \to \infty. \end{aligned}\tag{D2}$$

Hence, series $\{\mathfrak{b}_n^2\}$ diverges. It can be verified that $\{\mathfrak{b}_n\}$ diverges too. Now move to the condition when $\mu_{2i*} = \alpha \mathfrak{b}_i$. To find the extreme value of $\tilde{m} = \boldsymbol{\mu}\cdot\vec{\mathfrak{b}}/q$, we can write its Lagrange function L_a by

$$L_a = \boldsymbol{\mu}\cdot\vec{\mathfrak{b}} - \lambda(\boldsymbol{\mu}\cdot\boldsymbol{\mu} - C^2), \tag{D3}$$

whose bordered Hessian matrix $\mathbf{H}$ (denote $g = \boldsymbol{\mu}\cdot\boldsymbol{\mu}$) is

$$\mathbf{H}(L_a) = \begin{bmatrix} 0 & -\nabla_{\boldsymbol{\mu}} g \\ -\nabla_{\boldsymbol{\mu}} g^\intercal & \nabla_\mu \nabla_\mu L_a \end{bmatrix}. \tag{D4}$$

This matrix can be decomposed into $\mathbf{H}(L_a) = \mathbf{H}_A \cdot \mathbf{H}_B$, where

$$\begin{aligned}\mathbf{H}_A &= \begin{bmatrix} \mathbf{I} & -\nabla_{\boldsymbol{\mu}} g(\nabla_\mu \nabla_\mu L_a)^{-1} \\ \mathbf{0} & \mathbf{I} \end{bmatrix}, \\ \mathbf{H}_B &= \begin{bmatrix} -\nabla_{\boldsymbol{\mu}} g(\nabla_\mu \nabla_\mu L_a)^{-1}\nabla_{\boldsymbol{\mu}} g^\intercal & \mathbf{0} \\ \nabla_{\boldsymbol{\mu}} g^\intercal & \nabla_\mu \nabla_\mu L_a \end{bmatrix}. \end{aligned}\tag{D5}$$

Hence, the determinant can be computed by Schur's formula,

$$\det\mathbf{H} = -\det(\nabla_{\boldsymbol{\mu}}\nabla_{\boldsymbol{\mu}} L_a)\cdot\det[\nabla_\mu g(\nabla_{\boldsymbol{\mu}}\nabla_{\boldsymbol{\mu}} L_a)^{-1}\nabla_\mu g^\intercal], \tag{D6}$$

using the fact that $\nabla_{\boldsymbol{\mu}}\nabla_{\boldsymbol{\mu}} L_a$ is invertible due to

$$-\nabla_{\boldsymbol{\mu}} g = -2\boldsymbol{\mu}, \quad \nabla_{\boldsymbol{\mu}}\nabla_{\boldsymbol{\mu}} L_a = -2\lambda\mathbf{I}. \tag{D7}$$

The original bordered Hessian matrix has the following form:

$$\mathbf{H}(L_a) = -2\begin{bmatrix} 0 & \mu_{2*} & \mu_{4*} & \dots & \mu_{2n} \\ \mu_{2*} & \lambda & 0 & \dots & 0 \\ \mu_{4*} & 0 & \lambda & \dots & 0 \\ \vdots & \vdots & \vdots & \ddots & \vdots \\ \mu_{2n*} & 0 & 0 & \dots & \lambda \end{bmatrix}. \tag{D8}$$

Denote the left-upper $(j+1)\times(j+1)$ submatrix of $\mathbf{H}$ by ${}^j\mathbf{H}$, whose determinant can be computed by Eq. (D6):

$$-\frac{1}{2}\det{}^j\mathbf{H} = -\boldsymbol{\mu}\cdot\frac{1}{\lambda}\mathbf{I}_{j\times j}\cdot\boldsymbol{\mu}^\intercal = -\frac{1}{\lambda}\boldsymbol{\mu}\cdot\boldsymbol{\mu}. \tag{D9}$$

Another requirement we have is that $[\nabla_{\boldsymbol{\mu}} L_a\ \nabla_\lambda L_a] = \mathbf{0}$, where we can solve for Lagrangian multiplier

$$\lambda = \pm\frac{\sqrt{S}}{2C}, \quad \mu_{2i} = \pm\frac{C}{\sqrt{S}}\mathfrak{b}_i, \tag{D10}$$

where S is the summation of series $\{\mathfrak{b}_n^2\}$. If λ takes the negative value in Eq. (D10), then $\det{}^j\mathbf{H} < 0$ for every j. Therefore, the extreme value defined by Eq. (D10) when both λ and μ_{2i} are negative is a local minimum. So the symmetric point with respect to the origin gives the local maximum.

APPENDIX E: LANDSCAPE OF WINDING NUMBERS IN SEXTIC ANCHORING MODEL

In this Appendix, we will find the winding number W_p distribution in Λ_6, defined by the sextic anchoring model, discussed in Sec. IV B 2. The question is how prevalent or how scarce are parametric conditions that yield a high winding number of 3. In the quartic model the answer was relatively easy but for $n = 3$, the proliferation of polynomial roots creates challenges that require extensive analysis.

Winding number equals half of the number of waves of h, which corresponds to the distinct zeros inside the interval $\theta \in [-3\pi/2, \pi/2]$ of the polynomial $P[n] = \sum_{i=1}^{n/2} 2i\mu_{2i}\cos^{2i-1}\theta\sin\theta$.

If μ_4 and higher-order terms vanish, then $\theta = -3\pi/2, -\pi, -\pi/2, \pi/2$ are four trivial solutions, which corresponds to the one-wave pattern along $\mu_4 = 0$. And it is the fundamental reason why there are at least two waves within one period. If μ_4 does not vanish, then there are two other nontrivial solutions. Let $\mu_6 \neq 0$, then our problem is simplified to find all the roots of the following equation:

$$\mu_2 + 2\mu_4\cos^2\theta + 3\mu_6\cos^4\theta = 0, \tag{E1}$$

whose number of maximum root is eight (four available values for $\cos\theta$ by quartic equation, and each $\cos\theta$ value allows two possible θ). There are 12 roots in total including trivial solutions, corresponding to three-wavelength pattern profile. The general solution of Eq. (E1) is

$$\cos^2\theta = \frac{-\mu_4 \pm \sqrt{\mu_4^2 - 3\mu_2\mu_6}}{3\mu_6}. \tag{E2}$$

If we want to have the most wavelength patterns, then we need to make sure that $\mu_4^2 > 3\mu_2\mu_6$. If $\mu_4^2 = 3\mu_2\mu_6$ and at the same time $0 < -\frac{\mu_4}{3\mu_6} < 1$, then we have two-wavelength pattern; otherwise, we only have a one-wavelength pattern. Define this special surface as $\mathfrak{X}$. We already find the trivial roots when $\cos\theta = 0$ and 1. Since Λ_6 has central symmetry, we just need to evaluate three conditions.

1. sgn(μ)=(−, +, ±)

(i) If $\mu_6 > 0$, then

$$\mu_4 < \pm\sqrt{\mu_4^2 - 3\mu_2\mu_6} < \mu_4 + 3\mu_6, \tag{E3}$$

where $\pm$ can only take $+$ since $\mu_4 > 0$. Hence, we lose four roots. We can only have at most eight roots including trivial zeros, giving a two-wavelength pattern. After simplification we find that

$$\mu_6 > -\tfrac{1}{3}(\mu_2 + 2\mu_4) \text{ and } \mu_6 > 0. \tag{E4}$$

(ii) If $\mu_6 < 0$, then

$$\mu_4 > \pm\sqrt{\mu_4^2 - 3\mu_2\mu_6} > \mu_4 + 3\mu_6, \tag{E5}$$

where $\pm$ can take both $+$ and $-$. Hence, we discuss both conditions.

(iia) Keep $+$ in $\pm$. We can solve this inequality and denote the solution as W_{2+3}^{-+-}:

$$\left(\mu_6 < -\tfrac{1}{3}\mu_4\right) \cup \left\{\left(\mu_6 > -\tfrac{1}{3}\mu_4\right) \cap \left[\mu_6 > -\tfrac{1}{3}(\mu_2 + 2\mu_4)\right]\right\}.$$

(iib) Keep $-$ in $\pm$. We first need to ensure that $\mu_4 > -\sqrt{\mu_4^2 - 3\mu_2\mu_6}$, which is already true. On the other side we denote the solution as W_3^{-+-}:

$$\left[\mu_6 < -\tfrac{1}{3}(\mu_2 + 2\mu_4)\right] \cap \left(\mu_6 < -\tfrac{1}{3}\mu_4\right).$$

It is possible to keep both $+$ and $-$ in $\pm$ sign shown in Eq. (E2) by restricting $\boldsymbol{\mu}$ within $W_{2+3}^{-+-} \cap W_3^{-+-} = W_3^{-+-}$. Under this condition, we are able to obtain a three-wavelength pattern. And a two-wavelength pattern is obtained within $W_{2+3}^{-+-} \backslash W_3^{-+-}$. We see another two important surfaces: $\mathfrak{I}$: $\mu_6 = -\frac{1}{3}\mu_4$ and $\mathfrak{S} : \mu_6 = -\frac{1}{3}(\mu_2 + 2\mu_4)$. $\mathfrak{S}$ is shown in both conditions (i) and (ii), which ensures Eq. (E1) to have real roots since on this surface we have

$$\sqrt{\mu_4^2 - 3\mu_2\mu_6} = |\mu_2 + \mu_4|. \tag{E6}$$

Notice that Eq. (E2) looses four roots if $\mu_2 + \mu_4 = 0$, which is exactly the resonance line $\mathfrak{R}$ in Λ_4.

$\mathfrak{S}$ is the 2D version of critical line $\mathfrak{C}$ in Λ_6, since

$$\frac{dh}{d\theta} = -2\sin^3\theta\cos\theta[\sin^2\theta(\mu_2 + 2\mu_4) + \mu_2], \tag{E7}$$

and h shows a plateau area when $\theta \to 0 (qx \to \frac{\pi}{2})$. In addition, we should notice that the projection of $\mathfrak{S}$ on $\mu_2 - \mu_4$ plane is exactly $\mathfrak{C}$.

we are also interested in finding the 2D version of resonance line $\mathfrak{R}$, where six waves are identical. Resonance line requires

$$h\left(\theta + \frac{\pi}{3}\right) = h(\theta), \tag{E8}$$

which reduces to

$$\sum_{j=1,2,3} \frac{\mu_{2j}}{(2i)^{2j}}\left[\left(e^{\frac{i\pi}{3}}e^{i\theta} - e^{-\frac{i\pi}{3}}e^{-i\theta}\right)^{2j} - (e^{i\theta} - e^{-i\theta})^{2j}\right] = 0. \tag{E9}$$

Equation (E9) should hold true for every θ, from which we can conclude that there is no resonance surface (or line) in Λ_6. Hence, we cannot have six identical waves in μ_6 model. However,

$$\sum_{j=1,2} \frac{\mu_{2j}}{(2i)^{2j}}\left[\left(e^{\frac{i\pi}{2}}e^{i\theta} - e^{-\frac{i\pi}{2}}e^{-i\theta}\right)^{2j} - (e^{i\theta} - e^{-i\theta})^{2j}\right] = 0 \tag{E10}$$

reduces to

$$(\mu_2 + \mu_4)(\sin^2\theta - \cos^2\theta) = 0. \tag{E11}$$

Hence, $\mu_2 + \mu_4$ is the resonance line $\mathfrak{R}$ in Λ_4.

In summary, we conclude that there are three conditions when $\mu_2 < 0$ and $\mu_4 > 0$ where we get two-wavelength patterns. They are: (i) $\mu_4^2 = 3\mu_2\mu_6$ and $0 < -\frac{\mu_4}{3\mu_6} < 1$; (ii) if $\mu_6 > 0$, then $\mu_4^2 > 3\mu_2\mu_6$ and $\mu_6 > -\frac{1}{3}(\mu_2 + 2\mu_4)$; (iii) if $\mu_6 < 0$, then $\mu_4^2 > 3\mu_2\mu_6$ and $\mu_6 < -\frac{1}{3}(\mu_2 + 2\mu_4)$ and $\mu_6 < -\frac{1}{3}\mu_4$.

2. sgn(μ)=(+, −, ±)

First ensure that $\mu_4^2 > 3\mu_2\mu_6$.

(i) If $\mu_6 > 0$, then in Eq. (E3) we cannot eliminate any condition. Keep $+$ then we have $\mu_6 > -\frac{1}{3}(\mu_2 + 2\mu_4)$ and $\mu_6 > -\frac{1}{3}\mu_4$. Keep $-$ then we have $\mu_6 > -\frac{1}{3}\mu_4$ or $\mu_6 < -\frac{1}{3}\mu_4$ and $\mu_6 < -\frac{1}{3}(\mu_2 + 2\mu_4)$. Denote the following region as W_{2+3}^{+-+}:

$$\left(\mu_6 > -\tfrac{1}{3}\mu_4\right) \cup \left\{\left(\mu_6 < -\tfrac{1}{3}\mu_4\right) \cap \left[\mu_6 < -\tfrac{1}{3}(\mu_2 + 2\mu_4)\right]\right\}.$$

It is possible to have a three-wavelength pattern under the following condition, whose region being represented is denoted by W_3^{+-+}:

$$\left[\mu_6 > -\tfrac{1}{3}(\mu_2 + 2\mu_4)\right] \cap \left(\mu_6 > -\tfrac{1}{3}\mu_4\right).$$

Under the condition of $\mu_4^2 > 3\mu_2\mu_6$ (and $\mu_2 > 0, \mu_4 < 0$), $W_{2+3}^{+-+} \backslash W_3^{+-+}$ gives a two-wavelength pattern, and W_3^{+-+} gives a three-wavelength pattern.

(ii) If $\mu_6 < 0$, then in Eq. (E5) we can eliminate the condition of $+$ since $\mu_4 < 0$. So we can at most get a two-wavelength pattern. Solve for this inequality we find $\mu_6 < -\frac{1}{3}(\mu_2 + 2\mu_4)$.

In summary, we can observe this central symmetry between sgn($\boldsymbol{\mu}$) = (+, −, ±) and sgn($\boldsymbol{\mu}$) = (−, +, ±). The only difference between W_{2+3}^{+-+} and W_{2+3}^{-+-}, W_3^{+-+} and W_3^{-+-} is the direction of inequality sign.

3. sgn(μ)=(+, +, −)

Due to the existence of μ_6, it is also possible to obtain a two-wavelength pattern if both μ_2 and μ_4 have the same sign. Assume they are both positive. Then μ_6 can only be negative, and we have Eq. (E5), where $+$ is neglected since $-3\mu_2\mu_6 > 0$. Solving for this inequality we have $\mu_6 < -\frac{1}{3}(\mu_2 + 2\mu_4)$.

4. Parametric space Λ_6

Line $\mathfrak{S} \cap \mathfrak{I}$ is written as

$$\mathfrak{S} \cap \mathfrak{I} : \boldsymbol{\mu} = t\left[1, -1, \tfrac{1}{3}\right]. \tag{E12}$$

The intersection between $\mathfrak{S}$ and $\mathfrak{X}$ is

$$\mathfrak{S} \cap \mathfrak{X} : \boldsymbol{\mu} = t\left[1, -1, \tfrac{1}{3}\right]. \tag{E13}$$

Hence, $\mathfrak{S} \cap \mathfrak{I} = \mathfrak{S} \cap \mathfrak{X} := \mathfrak{r}$, which implies that $\mathfrak{S}$ is the tangent plane of $\mathfrak{X}$. Also notice that the projection of $\mathfrak{r}$ on Λ_4 is exactly $\mathfrak{R}$.

Therefore, $\mathfrak{X}$, $\mathfrak{S}$, and $\mathfrak{I}$ divide the small cube into six subregions as shown in Fig. 18. They are shown as black ($\mathfrak{X}$), blue ($\mathfrak{S}$), and green ($\mathfrak{I}$) surfaces in Figs. 18 and 19. The distribution of W_p under $(+++)$ and $(-++)$ are given in Fig. 18, while that under $(+-+)$ and $(--+)$ are provided by both front view and back view in Fig. 19. Let us look at Fig. 18 first, W_p can only be 1 under $(+++)$. Similarly, $W_p = 1$ under $(---)$ too. $W_p = 1$ only occurs in the small tetrahedron bounded by the cross-section between $\mathfrak{S}$ and small cube under $(-++)$.

Let us evaluate the distribution of W_p under $(--+)$ in Fig. 19. W_p can only be 1 or 2 under this condition. We can observe that $\mathfrak{S}$ is the boundary between the regions where $W_p = 1$ and $W_p = 2$, while $\mathfrak{I}$ does not affect W_p.

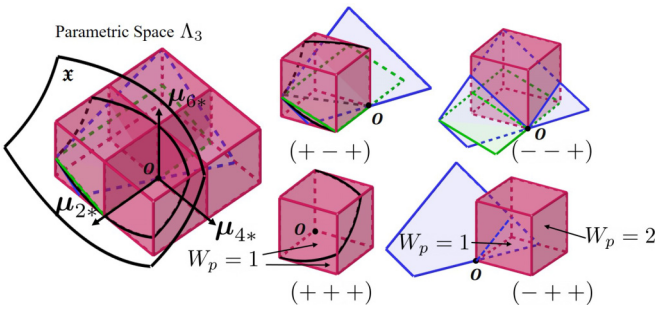

FIG. 18. The upper space of parametric space Λ_6 is composed by four small cubes showing on the right.

The distribution of W_p becomes very complicated under $(+-+)$ shown in Fig. 19. It can be proven that $\mathfrak{S}$, $\mathfrak{I}$ and $\mathfrak{X}$ intersect in the same line $\mathfrak{r}$, whose projection onto Λ_4 is exactly $\mathfrak{R}$, the resonance line in Λ_4. Hence, $\mathfrak{S}$ is the tangent plane to $\mathfrak{X}$ and the tangent line is $\mathfrak{r}$. Therefore, $\mathfrak{X}$, $\mathfrak{S}$ and $\mathfrak{I}$ separate the small cube $(+-+)$ to six regions. The region between $\mathfrak{X}$ and $\mathfrak{S}$ forces $W_p = 3$ and that below $\mathfrak{S}$ (2 small regions) requires $W_p = 2$. When $\boldsymbol{\mu}$ lies in the rest three regions one can only observe a winding pattern with $W_p = 1$.

We can see that under all the conditions $\mathfrak{S}$ is the boundary across which W_p jumps between two continuous natural number. It serves as a 2D version of critical line $\mathfrak{C}$ in Λ_4. This analogy becomes clearer when we notice that $\mathfrak{C} = \mathfrak{S} \cap \Lambda_4$. Although the projection of $\mathfrak{r}$ onto Λ_4 is $\mathfrak{R}$. There is no resonance surface (line) in Λ_6.

The reason that the winding number never changes its sign after a π rotation is that W_p, whose computation depends on $(\boldsymbol{\Xi}_\parallel, \boldsymbol{\Xi}_\perp)$, does not change sign after reversing the direction of $\mathbf{V} = [\boldsymbol{\mu}\ P_0]$. For example, the sign of the winding number of a simple Jordan curve can be computed by

$$\mathrm{sgn}(W_p) = (\mathbf{t}^\vee \wedge \mathbf{k}^\vee) \circ \left(\frac{\boldsymbol{\Xi}_\parallel}{|\boldsymbol{\Xi}_\parallel|} \bigwedge \frac{\boldsymbol{\Xi}_\perp}{|\boldsymbol{\Xi}_\perp|} \right) \tag{E14}$$

remains intact with the transformation $\boldsymbol{\mu} \to -\boldsymbol{\mu}$ or $P_0 \to -P_0$, where $^\vee$ represents the covector, $\wedge$ is the exterior product

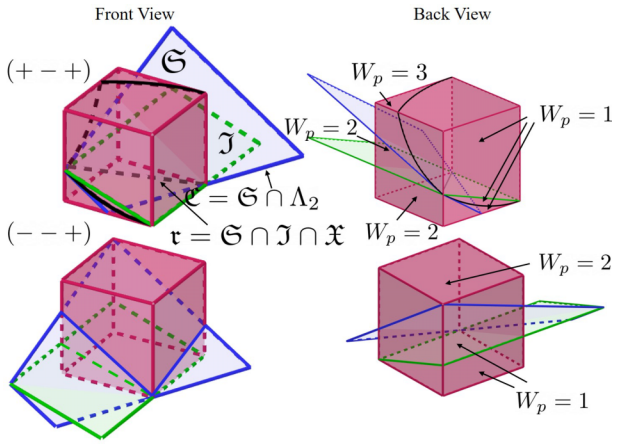

FIG. 19. Font view and back view of winding number W_p distribution of β under $(+-+)$ and $(--+)$ conditions.

and $\circ$ represents function composition. The verification is straightforward:

$$\begin{array}{ccc} \boldsymbol{\Xi}_\parallel \wedge \boldsymbol{\Xi}_\perp(\boldsymbol{\mu}, P_0) & \xrightarrow{-\Lambda_{2n}} & \boldsymbol{\Xi}_\parallel \wedge \boldsymbol{\Xi}_\perp(-\boldsymbol{\mu}, P_0) \\ \downarrow -\mathcal{P} & & \downarrow -\mathcal{P} \\ \boldsymbol{\Xi}_\parallel \wedge \boldsymbol{\Xi}_\perp(\boldsymbol{\mu}, -P_0) & \xrightarrow{-\Lambda_{2n}} & \boldsymbol{\Xi}_\parallel \wedge \boldsymbol{\Xi}_\perp(-\boldsymbol{\mu}, -P_0) \end{array}$$

where four quantities stated above are totally identical since the negative sign canceled naturally due to the invariance of $(\mathbf{t}^\vee \wedge \mathbf{k}^\vee)$. There is also an intuitive explanation. $\boldsymbol{\Xi}_\parallel \wedge \boldsymbol{\Xi}_\perp$ defined the direction (before scaling to unit) of mechanical frame, while $\mathbf{t} \wedge \mathbf{k}$ indicates the direction of geometric frame. Therefore, The invariance of $\mathrm{sgn}(W_p)$ actually implies that the transformation between geometric frame and mechanical frame preserves the direction and is independent to the position on the surface.

In summary, this Appendix shows that in the sextic model one find high winding numbers in the $(+-+)$ and $(-++)$ anchoring conditions.

APPENDIX F: $\boldsymbol{\phi} - \boldsymbol{\Xi}_\parallel$ RELATION

This Appendix is to derive the explicit formula to evaluate surface normal angle ϕ as a function of $\Xi_\parallel$ when $\mu_4 = 0$, given in Eq. (57). From Eq. (55), we can solve $\Xi_\perp$:

$$\Xi_\perp = \mathcal{C}_0 \pm \frac{1}{2}\sqrt{\mu_2^2 - \Xi_\parallel^2}. \tag{F1}$$

From Eq. (26), we can solve that ϕ is expressed by

$$\phi = \frac{\pi}{2} + \underbrace{\int_0^x \frac{1}{\Xi_\perp} \partial_x \Xi_\parallel \, dx}_{I_1}. \tag{F2}$$

Now replace $\Xi_\perp$ and evaluate I_1^+ and I_1^- for the $+$ or $-$ sign in Eq. (F1):

$$\begin{aligned} I_1^+ &= \int_0^{\Xi_\parallel} \frac{1}{\mathcal{C} + \frac{1}{2}\sqrt{\mu_2^2 - \Xi_\parallel^2}} \, d\Xi_\parallel = 2\int_0^{\arcsin \frac{\Xi_\parallel}{\mu_2}} d\Psi \\ &\quad - 2\underbrace{\int_0^{\arcsin \frac{\Xi_\parallel}{\mu_2}} \frac{1}{1 + k\cos\Psi} \, d\Psi}_{I_2^+}, \end{aligned} \tag{F3}$$

where $k = \frac{\mu_2}{2\mathcal{C}}$ and $\Psi = \arcsin \frac{\Xi_\parallel}{\mu_2}$. Evaluate I_2^+ and replace $v = \tan\frac{\Psi}{2}$, further replace $t = v\sqrt{\frac{1-k}{1+k}}$.

$$\begin{aligned} I_2^+ &= \int_0^{\tan(\frac{1}{2}\arcsin\frac{\Xi_\parallel}{\mu_2})} \frac{1}{1 + k\left(\frac{1-v^2}{1+v^2}\right)} \cdot \frac{2}{1+v^2} \, dv \\ &= \frac{2}{1+k}\int_0^{\tan(\frac{1}{2}\arcsin\frac{\Xi_\parallel}{\mu_2})} \frac{1}{\left(\frac{1-k}{1+k}\right)v^2 + 1} \, dv \end{aligned}$$

$$= \frac{2}{1+k}\int_0^{\sqrt{\frac{1-k}{1+k}}\tan\left(\frac{1}{2}\arcsin\frac{\Xi_\parallel}{\mu_2}\right)} \frac{1}{t^2+1}\,dt \cdot \frac{1}{\sqrt{\frac{1-k}{1+k}}}$$

$$= \frac{2}{\sqrt{1-k^2}}\arctan\left[\sqrt{\frac{1-k}{1+k}}\tan\left(\frac{1}{2}\arcsin\frac{\Xi_\parallel}{\mu_2}\right)\right]. \quad \text{(F4)}$$

Therefore, combine all the results and replace k with $\frac{\mu_2}{2\mathcal{C}}$, so we get

$$\phi^+ = \frac{\pi}{2} + 2\arcsin\frac{\Xi_\parallel}{\mu_2} - \frac{2(2+\mu_{2*})}{\sqrt{1+\mu_{2*}}} \times \arctan\left[\frac{1}{\sqrt{1+\mu_{2*}}}\tan\left(\frac{1}{2}\arcsin\frac{\Xi_\parallel}{\mu_2}\right)\right]. \quad \text{(F5)}$$

Now we evaluate I_1^-:

$$I_1^- = \int_0^{\Xi_\parallel} \frac{1}{\mathcal{C} - \frac{1}{2}\sqrt{\mu_2^2 - \Xi_\parallel^2}}\,d\Xi_\parallel = -2\int_0^{\arcsin\frac{\Xi_\parallel}{\mu_2}} d\Psi + 2\underbrace{\int_0^{\arcsin\frac{\Xi_\parallel}{\mu_2}} \frac{1}{1-k\cos\Psi}\,d\Psi}_{I_2^-}. \quad \text{(F6)}$$

Replace $\alpha = \Psi + \pi$ such that

$$I_2^- = \int_0^{\arcsin\frac{\Xi_\parallel}{\mu_2}+\pi} \frac{1}{1+k\cos\alpha}\,d\alpha. \quad \text{(F7)}$$

Equation (F7) allows us to transform I_2^- to be the same as I_2^+, we can use the result directly:

$$I_2^- = -\frac{2}{\sqrt{1-k^2}}\arctan\left[\sqrt{\frac{1-k}{1+k}}\cot\left(\frac{1}{2}\arcsin\frac{\Xi_\parallel}{\mu_2}\right)\right]. \quad \text{(F8)}$$

Hence, corresponding ϕ^- can be computed by

$$\phi^- = \frac{\pi}{2} - 2\arcsin\frac{\Xi_\parallel}{\mu_2} - \frac{2(2+\mu_{2*})}{\sqrt{1+\mu_{2*}}} \times \arctan\left[\frac{1}{\sqrt{1+\mu_{2*}}}\cot\left(\frac{1}{2}\arcsin\frac{\Xi_\parallel}{\mu_2}\right)\right]. \quad \text{(F9)}$$

[1] P. J. Willcox, S. P. Gido, W. Muller, and D. L. Kaplan, Macromolecules **29**, 5106 (1996).
[2] M. Mitov, Soft Matter **13**, 4176 (2017).
[3] A. D. Rey, Soft Matter **6**, 3402 (2010).
[4] A. P. C. Almeida, J. P. Canejo, S. N. Fernandes, C. Echeverria, P. L. Almeida, and M. H. Godinho, Adv. Mater. **30**, 1703655 (2018).
[5] N. Noroozi and D. Grecov, J. Non-Newton Fluid **208**, 1 (2014).
[6] V. Sharma, M. Crne, J. O. Park, and M. Srinivasarao, Mater. Today: Proc. **1**, 161 (2014).
[7] F. Carrión, G. Martínez-Nicolás, P. Iglesias, J. Sanes, and M. Bermúdez, Int. J. Mol. Sci. **10**, 4102 (2009).
[8] B. Jerome, Rep. Prog. Phys. **54**, 391 (1991).
[9] H. Yokoyama and H. A. van Sprang, J. Appl. Phys. **57**, 4520 (1985).
[10] A. D. Rey, Soft Matter **3**, 1349 (2007).
[11] P. Rofouie, Z. Wang, and A. D. Rey, Soft Matter **14**, 5180 (2018).
[12] Z. Wang, P. Rofouie, and A. D. Rey, Crystals **9**, 190 (2019).
[13] A. Cheong and A. D. Rey, Liquid Crystals **31**, 1271 (2004).
[14] A. D. Rey, Phys. Rev. E **69**, 041707 (2004).
[15] A. G. Cheong and A. D. Rey, Phys. Rev. E **66**, 021704 (2002).
[16] D. W. Hoffman and J. W. Cahn, Surf. Sci. **31**, 368 (1972).
[17] R. W. Ogden, Q. Appl. Math. **44**, 255 (1986).
[18] J. G. Ramsay and M. I. Huber, *The Techniques of Modern Structural Geology: Folds and Fractures* (Academic Press, San Diego, CA, 1987).
[19] Y. K. Murugesan, D. Pasini, and A. D. Rey, Soft Matter **9**, 1054 (2013).
[20] P. Rofouie, D. Pasini, and A. D. Rey, Soft Matter **11**, 1127 (2015).
[21] P. Rofouie, D. Pasini, and A. D. Rey, Soft Matter **13**, 541 (2017).
[22] B. Bhushan, *Modern Tribology Handbook* (CRC Press, Boca Raton, FL, 2001).
[23] S. D. Cho, P. Rajitrangson, B. A. Matis, and J. A. Platt, Oper. Dent. **38**, E58 (2013).
[24] A. Riveiro, A. L. B. Maçon, J. del Val, R. Comesaña, and J. Pou, Front. Phys. **6**, 16 (2018).
[25] M. F. Ayad, N. Z. Fahmy, and S. F. Rosenstiel, J. Prosthet. Dent. **99**, 123 (2008).
[26] W. K. Schief, A. Szereszewski, and C. Rogers, J. Math. Phys. **48**, 073510 (2007).
[27] H. M. Whitney, M. Kolle, P. Andrew, L. Chittka, U. Steiner, and B. J. Glover, Science **323**, 130 (2009).
[28] X. Feng, A. Mourran, M. Möller, and C. Bahr, ChemPhysChem **14**, 1801 (2013).
[29] A. D. Rey, J. Chem. Phys. **110**, 9769 (1999).
[30] P. Yue, J. J. Feng, C. Liu, and J. Shen, J. Colloid Interface Sci. **290**, 281 (2005).
[31] R. Meister, H. Dumoulin, M.-A. Hallé, and P. Pieranski, J. Phys. II France **6**, 827 (1996).
[32] C. M. Bidan, K. P. Kommareddy, M. Rumpler, P. Kollmannsberger, P. Fratzl, and J. W. C. Dunlop, Adv. Healthc. Mater. **2**, 186 (2013).
[33] A. Rapini and M. Papoular, J. Phys. Colloq. **30**, C4 (1969).
[34] A. A. Sonin, *The Surface Physics of Liquid Crystals* (Gordon and Breach Publishers, London, UK, 1995).
[35] I. W. Stewart, *The Static and Dynamic Continuum Theory of Liquid Crystals: A Mathematical Introduction* (CRC Press, Boca Raton, FL, 2003).
[36] A. D. Rey, J. Chem. Phys. **120**, 2010 (2004).
[37] A. D. Rey, Phys. Rev. E **60**, 1077 (1999).
[38] A. D. Rey, Phys. Rev. E **61**, 1540 (2000).
[39] A. D. Rey, Langmuir **22**, 219 (2006).
[40] P. Rofouie, D. Pasini, and A. D. Rey, J. Chem. Phys. **143**, 114701 (2015).

[41] A. D. Rey, J. Chem. Phys. **111**, 7675 (1999).
[42] O. F. A. Gutierrez and A. D. Rey, Soft Matter **14**, 1465 (2018).
[43] B. Bhushan, *Introduction to Tribology* (John Wiley & Sons, New York, NY, 2013).
[44] J. R. Munkres, *Topology* (Prentice-Hall, Upper Saddle River, NJ, 2000).
[45] E. V. Shikin, *Handbook and Atlas of Curves* (CRC Press, Boca Raton, FL, 1995).
[46] A. Urzica and S. Cretu, J. Balk. Tribol. Assoc. **19**, 391 (2013).
[47] N. Tayebi and A. A. Polycarpou, Tribol. Int. **37**, 491 (2004).
[48] D. K. Wainwright, G. V. Lauder, and J. C. Weaver, Methods Ecol. Evol. **8**, 1626 (2017).
[49] M. Forest, P. Phuworawong, Q. Wang, and R. Zhou, Phil. Trans. R. Soc. A **372** (2014).
[50] A. Sokolov, A. Mozaffari, R. Zhang, J. J. de Pablo, and A. Snezhko, Phys. Rev. X **9**, 031014 (2019).
[51] J. Zhao, U. Gulan, T. Horie, N. Ohmura, J. Han, C. Yang, J. Kong, S. Wang, and B. B. Xu, Small **15**, 1900019 (2019).
[52] H. R. Brand, H. Pleiner, and D. Svenšek, Rheol. **57**, 773 (2018).
[53] D. A. Beller, M. A. Gharbi, A. Honglawan, K. J. Stebe, S. Yang, and R. D. Kamien, Phys. Rev. X **3**, 041026 (2013).
[54] E. G. Virga, *Variational Theories for Liquid Crystals* (Routledge, Oxford, 2018).
[55] W. Gautschi, J. Math. Phys. **38**, 77 (1959).